Synthesis of Bioactive Glasses SiO2-Al2O3-MgO-K2CO3-CaO-MgF2 -CNT: Structural, Mechanical and Biological Properties

Dr. chandkiram Gautam (gautam_ceramic@yahoo.com)
University of Lucknow https://orcid.org/0000-0003-3190-5577

Shweta .
University of Lucknow Faculty of Science

Krishna Kishor Dey
Dr Hari Singh Gour University

Manasi Ghosh
Banaras Hindu University

Ravi Prakash
CDRI: Central Drug Research Institute

Kriti Sharma
CDRI: Central Drug Research Institute

Divya Singh
CDRI: Central Drug Research Institute

Research Article

Keywords: Bioactive Glasses, Structural Properties, NMR spectroscopy, Mechanical properties, Contact angle, Cell viability

Posted Date: May 5th, 2021

DOI: https://doi.org/10.21203/rs.3.rs-479436/v1

Synthesis of Bioactive Glasses SiO_2-Al_2O_3-MgO-K_2CO_3-CaO-MgF_2 -CNT: Structural, Mechanical and Biological Properties

Chandkiram GAUTAM[a,*], Shweta[a,*], Krishna Kishor DEY[b], Manasi GHOSH[c], Ravi PRAKASH[d], Kriti SHARMA[d], Divya SINGH[d]

[a]*Advanced Glass and Glass Ceramics Research Laboratory, Department of Physics, University of Lucknow, Lucknow, Uttar Pradesh-226007 (India)*
[b]*Department of Physics, Dr. Harisingh Gour Central University, Sagar, Madhya Pradesh-470003 (India)*
[c]*Physics Section, MMV, Banaras Hindu University, Varanasi-221005, UP, India*
[d]*Endocrinology Division, CSIR-Central Drug Research Institute, Lucknow-226031 (India)*
[*]*E-mail: gautam_ceramic@yahoo.com*

Abstract: Six glass compositions were synthesized using a melt quenching technique reinforced with different concentrations of carbon nanotubes (CNTs) from 0.1 to 0.7% in the glassy system SiO_2-Al_2O_3-MgO-K_2CO_3-CaO-MgF_2. Density and molar volumes were estimated by employing a liquid displacement method. In the present study, the reinforcement effect of CNTs was explained using several spectroscopic techniques i.e. Fourier transform infrared (FTIR), ultraviolet-visible (UV-Vis), Raman, and nuclear magnetic resonance (NMR) spectroscopy respectively. Based on Tauc plots of the UV-Vis spectra, the energy band gap was determined and their values decreased from 4.33 to 3.9 eV. Contact angle measurements were performed to check the wettability of the glasses. ^{29}Si-MAS-NMR spectroscopic study showed the random distribution of two dissimilar Ca^{2+} and Mg^{2+} ions within these glasses which lead to structural and topological frustration. To check the cell viability, MTT and alkaline phosphatase (ALP) assay were also performed. Owing to outstanding stability in various fluids like saline water, distilled water, and hydrochloric acid, the synthesized glasses exhibited functional activities with an adequate proliferation of rat calverail osteoblast (ROB) cell. Consequently, based on the various characterization techniques such as

mechanical, tribological, and biological activities, the fabricated bioactive glassy material can be used for biomedical and multifunctional applications.

Keywords: Bioactive Glasses; Structural Properties; NMR spectroscopy; Mechanical properties; Contact angle; Cell viability.

1 Introduction

The bioactive glass and glass ceramics are extensively used in bone/tissue repair and being developed for many tissue engineering applications [1-5]. Bioactive glass also revealed an amorphous structure similar to an ordinary glass, while glass ceramics are crystallized glasses, containing a composite of a crystalline phase as well as a residual glassy phase. Hench et al. were the first to reveal the excellent bioactivity property of the bioglass, which attracted much attention to the research for various biomedical applications such as bone implants, tooth implants, etc. [4]. Moreover, bioactive glass has a unique tendency to bond with natural bone. These glasses act as a catalyst for the healing process which is demonstrated by clinical studies [6,7]. Bioactive glass particularly is a bioceramic material that widely being investigated for bone regeneration applications in orthopedic and orthodontics [8]. The bioactivity of a bioglass can be enhanced by the formation of an apatite layer on the surface [8]. It is reported that bioglass has a strong tendency to form bonds with soft connective tissues and bone [9]. So, owing to their high biocompatibility, low cost and bioactivity, they are widely being used for numerous biomedical applications [4,10,11]. Besides, owing to deficiency of antibacterial property in bioglass; they have a severe drawback in surgery due to bacterial infection [12-15]. Thus, scientists are paying much attention to develop such a bioactive glass which is highly suitable for the restoration of bone/teeth and also can avoid all the adverse effects. The most used glassy material for biomedical applications is 45S5 Bioglass [11,16]. So, there is keen interest in the research area of biomedical science over

the past two decades, as demonstrated by the increasing number of bioactive glasses, $45SiO_2$-$24.5Na_2O$-$24.5CaO$-$6P_2O_5$, 45S5 Bioglass®, (16.20-*x*)MgO-*x*Na_2O-37.14CaO-3.62P_2O_5-42.46SiO_2-0.58CaF_2, polycaprolactone (PCL)-45S5 Bioglass® etc. [4,17-22]. Since the bone-bonding properties of 45S5 Bioglass® approximately 40 years ago were reported and still a lot of research work under progress for the development of highly biocompatible glass and glass ceramics [23]. Moreover, this is a silicate based three-dimensional (3-D) glass-forming SiO_2 network in which silicon (Si) is fourfold coordinated with each oxygen atom (O). The main compositional structures played substantial role for bioactivity of 45S5 glasses such as less concentration of SiO_2, high content of glass network modifiers Na_2O and CaO, and high CaO/P_2O_5 ratio. The biocompatibility and bone bonding mechanism of 45S5 glass has been studied in detail [24,25].

So, based on the above studies, the bonding between 45S5 glass and bone was recognized to the creation of carbonate replaced hydroxyapatite (HAp) like layer on the surface of bioglass when it comes in contact with body fluid. The 45S5 silicate bioactive glass composition (45% SiO_2-24.5% Na_2O-24.5% CaO-6% P_2O_5 (wt %)) has a reasonably larger amount of SiO_2 and other network modifiers, like K_2O and MgO, when compared to 45S5. Recently it has been reported that few compositions in other glassy compound e.g. borate glasses [26-30] are also known as bioactive ceramics. Due to their inferior chemical durability, few borate bioactive glasses (BBGs) degrade faster and act like a HAp material, in comparison to silicate based 45S5 glass [24,25,31,32]. More recently, Hong Li et al. synthesized a glass composition of SiO_2 40%, Al_2O_3 12%, MgO 10%, MgF_2 24%, CaO 5%, K_2O 1%, ZrO_2 8% (wt%) for dental CAD/CAM application [33].

Although, reactivity as well as solubility modification intensely at network connectivity by 2, that is the state where structure of the glass changes from a crosslinked network to linear chains.

Lower the network connectivity of a glass, lower its glass transition temperature and enhance its reactivity along with solubility simultaneously. Consequently, network connectivity (NC) is very supportive for the fabrication of a new bioactive glassy compound. It has already been reported that the natural bone mainly consists water content of (10%), organic material (20%) and other mineral matter (70%) [34]. In case of certain injury, if the bone or its part is lost then bone grafting can be done as it serves for both biological as well as mechanical applications [35]. Hench and Wilson were reported two main features that should be presented in a bioglass: (1) a stable interface should be formed among the material and natural tissues and (2) the mechanical properties should be the same or better as the replaced tissues [36]. Hence, bioglass is suitable ceramic material for bone regeneration as the mineral ingredients of the bone is approximately the same as the chemical composition of the apatite layer [8].

Further, carbon is a naturally occurring material found in various forms and suitable for many technological applications due to its wide range of properties [37]. Carbon nanotubes (CNTs) have small dimensions, superior mechanical strength, aspect ratio and stiffness [35]. Nowadays, this material was used for various applications like aerospace, energy generation, electronics, etc [38]. Sumo Ijima et al. in 1991 have been reported the various forms of carbon structure as CNT and revealed its significant electrical conductivities, high aspect ratio, flexibility including adequate mechanical strength [39,40]. Moreover, its derivative is called graphene which has a single layer carbon nanosheet and exhibits excellent mechanical, thermal, optical and biological properties. Thus, CNT can be formed by rolling a graphene nanosheet in cylindrical shape (1-D) [41]. Webster and its co-workers had firstly reported in 2002 that nano-carbon material can be used for biomedical osteoblast differentiation [37]. CNT has an ordered structure material due to which has excellent antimicrobial and mechanical properties. Besides its excellent electrical

conductivities, high aspect ratio, flexibility and adequate mechanical strength, CNT has several other applications for the fabrication of many devices such as optical devices, superconducting, molecular switches including biomedical devices [42]. So, owing to its large surface area, excellent biocompatibility and adequate mechanical strength, CNT can be utilized for several biomedical applications [43,44]. Researchers found to be enough interaction among CNTs and cells and reported that carbon nanostructures of nanofibers, diamond, and fullerene, etc. can also be used for biomedical applications [45]. Meng et al. were studied a ternary ceramic composite system HAp-ZrO_2-CNT by using a hot-press sintering technique. In this study, they reported good biocompatibility and enhanced flexural strength and fracture toughness by ~126% and ~124%, respectively than that of unmodified HAp [46]. It has been reported that the addition of multi walled carbon nanotubes (MWCNTs) to the 3-D bioglass, enhanced the compressive strength and bioactivity significantly [47, 48]. Further, Armentano et al. have been studied in vitro bio-mineralization processes on human alveolar bone-derived cells using carboxylated and fluorinated single wall nanotube (SWNT) films. In this study, they demonstrated an encouraging biocompatibility and gene expression with cell phenotypes that can be regulated easily [49]. However, Zanello et al. have compared the osteoblast cell formation and bone creation using functionalized and non-functionalized CNTs [50]. Khang et al. had studied the articular cartilage tissue regeneration using a carbon nanotube/polycarbonate urethane film [51]. Further, Yu Xiao et al. have studied the functionalized MWCNTs via in situ deposition of HAp to enhance their hydrophilicity as well as biocompatibility [52]. Ya-Ping Guo et al. synthesized carbonated HAp/CNT coatings with mesoporous structures, and then macro powders and CNTs were electrophoretically deposited on a substrate using a microwave irradiation technique [53]. The achieved coatings comprising mesoporous structure (pore sizes ~3.9 nm), and reveal an excellent

in vitro bone developing activity. In this research paper our aim is to explore the structural networking between different glass former and network modifier due to the variation of CNT concentration on structural, mechanical, and biological properties of the synthesized glassy system SiO_2-Al_2O_3-MgO-K_2CO_3-CaO-MgF_2-CNT. The glass sample GCNT0.7 can be used for various biomedical applications.

2 Experimental procedures

2.1 Glass sample preparation

Various glass compositions were melted from their raw materials especially using high purity chemicals i.e. SiO_2, Al_2O_3, MgO, K_2CO_3, CaO, MgF_2 (Merck USA) and CNT (Sigma Aldrich, USA) in batches of 20 to 40 gm in a highly pure alumina crucible. The total mole amount of the glass composition is set to be 100% for superior comparison. The batch compositions, density, molar volume, optical band gap and contact angle of the base glass samples are listed in Table 1. All the glasses were reinforced with different content of CNT (0.1 - 0.7 mol %) and melts were kept for 2 h @ 1450 ^oC to improve its homogeneity. The glass melt was cast into a brass block mould (2x4 cm); pressed by another brass plate and then quickly replaced into a preheated programmable electric muffle furnace for annealing @ 450 ^oC for 4 h to release residual internal stress and then annealed glass samples taken out from this furnace at room temperature. Eventually, the prepared glass samples were cut and polished for further characterizations.

2.2 XRD measurements

For XRD measurements, glass samples were ground with the help of a mortar pestle to achieve a fine powder. Further, XRD patterns have been recorded on powdered glass samples using a Rigaku Miniflex-II X-ray diffractometer employing Cu-Kα radiation comprising the

wavelength of ~1.54056 Å for the confirmation of amorphous nature over a 2Θ range from 20° to 80° and X-ray tube was operated at 40 kV and 40 mA.

2.3 Density and molar volume

Density of glass samples depends upon varied concentrations of CNT as well as on compositional changes. Thus, the density of all glasses was calculated using Archimedes' principle [54]. Doubled distilled water was utilized and density was measured using a weighing digital balance possessing accuracy up to 0.0001 mg. The measurements of density were carried out thrice for each glass sample. The average values of the density measurements are shown in Table 1. The maximum random variation in the density measurements was 0.001 g/cm^3. Therefore, the densities (ρ) and molar volumes (V_M) of the CNT doped glass samples were calculated using the following formulae [55,56]

$$\rho = \frac{W_2 - W_1}{(W_4 - W_1) - (W_3 - W_2)} \rho_w \tag{1}$$

where, ρ is the density (g/cm^3), ρ_w is the density of distilled water (1 g/cm^3), W_1 = weight of empty specific gravity bottle (g), W_2 = weight of specific gravity bottle with sample (g), W_3 = weight of specific gravity bottle with sample and distilled water (g), and W_4 = weight of specific gravity bottle with distilled water (g), and:

$$V_M = \frac{\sum X_i M_i}{\rho} \tag{2}$$

where, M_i is the molecular weight of ith factor and X_i is the molar portion of the ith component.

2.4 Fourier Transform Infrared (FTIR) Spectroscopy

FTIR absorption spectra of the annealed glass samples were obtained at room temperature within the wavenumber range of 4000 - 600 cm^{-1} using a JASCO FT/IR-5300. Samples were grinded into fine powder (<180 μm) and then mixed with KBr powder in the ratio of 1:9 precisely.

Subsequently, the powdered mixtures were pressed uniaxially using a hydraulic press machine to form clear homogeneous discs. The prepared discs of the various glass samples were dried at 150 ^{o}C for 1 h in an oven to remove the moisture.

2.5 UV–vis spectroscopy

UV-vis spectroscopy of the all glass samples was also carried out using UV-Vis spectrophotometer (Shimadzu, UV-2450) within the wavelength of 200 - 1000 nm and spectral resolution of 0.2 nm. The values of optical energy band gap was determined for the fabricated glass samples from the plots of Mott and Davis relationship which studies the absorption coefficient, α, and photon energy, E [57,58]:

$$\alpha = \frac{\left(h\nu - E_g\right)^n}{h\nu} \tag{3}$$

where, α denotes the absorption coefficient, $h\nu$ is the photon energy, the constant n depends on the type of transition (n = 1/2 for allowed direct transition and n = 2 for allowed indirect transition), and E_g is the band gap energy of the samples. α was determined at different photon energies by the formulae: $\alpha = A/d$, where A represents absorbance while d represents the thickness of the samples. Herein, the values of direct optical band gap, E_g, was calculated using inducing the linear part of the curves of $(\alpha h\nu)^{1/2} = 0$ and the curve of $(\alpha h\nu)^{1/2}$ versus $h\nu$.

2.6 Raman Spectroscopy

Raman measurements were performed by employing a Raman spectroscopy (micro-Raman setup, Renishaw, Gloucestershire, UK) furnished by a grating of 1800 lines/mm as well as an Olympus (Model: MX50 A/T; Olympus, Hamburg, Germany) A/T was equipped with a spectrometer in order to focus laser light on the glass sample which gathers the scattered light at 180^{o}. Further, an Argon (Ar+) laser having a wavelength of the order of 514.5 nm has been used

with a Spex 1404 double monochromator and GRAM-32 (Adept Scientific plc., Hertfordshire, UK) software for recording the data. In this way, Raman spectra of all powdered glass samples were taken in the wavenumber range of 2000 - 30 cm^{-1}.

2.7 Nuclear Magnetic Resonance (NMR) Measurements

^{29}Si magic angle spinning (MAS) Solid State NMR experiments were performed on JEOL ECX 500 NMR Spectrometer (housed at Dr. Harisingh Gour Central University, Sagar, India). The spectrometer was decorated by a 3.2 mm JEOL double resonance MAS probe. ^{29}Si MAS-NMR tests were carried out using a sample spinning speed of 10 kHz. Reference for ^{29}Si chemical shifts measurements were done by using 2,2-dimethul-2-silapentane-5-sulfonate sodium salt (DSS). For getting ^{29}Si MAS NMR spectra a 90^0 pulse width of 3 μs was also used by a relaxation delay of 30 s.

2.8 Contact Angle Measurements

Small glass samples were taken for contact angle measurements with dimensions of 3 mm x 5 mm x 8 mm. Glass samples were ground and polished successively using different mesh size of SiC powders along with diamond paste (1 μm). The polished glass samples were thoroughly cleaned using ethanol solution and then dried in an oven @ 100 ^oC for 20 min to eliminate the moisture from the polished glass samples. The contact angle tests were also performed on these well-polished glass samples using Rame-hart, Inc. (Imaging System, Mountain Lakes, NJ, USA). A drop of deionized water is carefully placed on the polished surface of the glass sample using a hypodermic syringe needle. The photographs of drops were taken quickly by a high-resolution digital camera just after putting the drop of water on the sample. The drop volume was controlled within the range from 10~20 µL [59]. Contact angles of the all polished glass samples were measured by using "ImageJ" software and their values are listed in Table 1.

2.9 Dynamical Mechanical Analysis (DMA) Measurements

DMA measurements were performed to determine storage modulus and strain properties of three selected glass samples. DMA accepts several different forms of the samples. Equipment available for this study required small rectangular samples approximately dimensions of 1.3 mm x 5 mm x 8 mm. Dimensions of all sample were measured by DMA and further confirmed using a digital caliper. Dynamic mechanical testing was carried out in compression mode using TA Instruments Q800 DMA at room temperature. Parameters were chosen based on review of literature and discussions with experienced DMA researchers.

2.10 Scanning Electron Microscopy

The surface morphology of the fine powdered glass samples was observed using a scanning electron microscope (model: JEOL JSM-6400). Glass samples were ground to make the fine powder using a mortar and pestle. For the recording of SEM images, the tiny amount of fine powdered glass samples was taken on to a copper stub and then coated with Ag-Pd thin films using a sputtering machine 'JEOL, JEC-3000FC Auto Fine Coater' to avoid the charge build-up on them. Finally, the achieved samples along with stubs were then mounted in a sample holder by a conducting carbon tape and hence, SEM images were recorded at desired magnifications.

2.11 Biological Activities

2.11.1 MTT Assay for cell viability

To evaluate the capability of the osteoblast cells in presence of the fine powdered samples GCNT0.1 and GCNT0.7 (containing the lowest and higher amount of CNT), rat calverail osteoblast (ROB) cells were extracted from mouse pups calvaria culture and on 90% confluency, cells were reseeded in 96 well plates. After 24 h, different concentrations of these samples were given to the cells and then incubated for 48 h at 37 °C in a moistened atmosphere containing 5%

CO_2 and 95% air. After the incubation period, MTT reagent (5 mg/ml) was added and the plate was incubated further at 37 °C for 3 – 4 h to form the formazan crystals. After the end of incubation, dimethyl sulfoxide (DMSO) was added to dissolve the crystals and optical density (OD) was estimated at 570 nm [60].

2.11.2 Alkaline phosphatase (ALP) assay for osteoblast differentiation

For evaluation of the osteogenic activity of this compound, alkaline phosphatases assay was being carried out on the osteoblast cells extracted from mouse pups calvarial tissue. Osteoblast cells at 90% confluence were trypsinized and reseeded in the 96 well plate (2×10^3 cells per well) in 10% alpha-MEM medium. After 24 h, cells were treated with varying contents of glass samples GCNT0.1 and GCNT0.7 in osteoblast differential medium (α-MEM supplemented with 5% FBS, 10 nM b-glycerophosphate, 50 mg/ml ascorbic acid and 1% penicillin/streptomycin) and plates were incubated for 48 h at 37°C in a moistened atmosphere of 5% CO_2 and 95% air. After incubation, entire ALP activity was studied using the substrate p-nitrophenylphosphate (PNPP) and then quantified calorimetrically at 405 nm [61,62].

2.11.3 Stability in saline water, distilled water and hydrochloric acid (HCL)

To check the stability in physiological conditions, weight loss tests were also performed on the fabricated glass samples at room temperature using different solvent i.e. the saline water (Sodium Chloride Injection IP (0.9% w/v) made by Tara Bioscience Pvt. Ltd. (India), distilled water and hydrochloric acid (MERCK). Glass samples were then dipped into this solution for 8 h, 8h and 3h soaking time respectively. Moreover, the weight differences were measured before and after the treatment with saline water, distilled water and hydrochloric acid respectively by a weighing digital balance that contained an accuracy up to 0.0001 mg and thus obtained data was analyzed successfully.

3 Results and Discussion

3.1 XRD analysis

XRD patterns of the glass samples GCNT0.1, GCNT0.2, GCNT0.3, GCNT0.4, GCNT0.5 and GCNT0.7 are shown in Figure 1 respectively. These XRD patterns depicted a broad diffuse peak instead of sharp crystalline peak which endorsing a typical long-range structural disorder of an amorphous material. The XRD patterns of these glass samples showed almost similar behaviors and confirmed the pure unstructured nature of the fabricated glasses.

3.2 Density and molar volume analysis of the glass samples

Density of the fabricated annealed glass samples was calculated and listed in Table 1. From Table 1, it has been noticed that the calculated values of density decrease with rising doping content of CNT. The values of density of all glass samples were found to be in the range of 1.99 - 2.98 gm/cc. It is also due to the decreasing content of CaO (2.65 gm/cc). So, due to this decreasing content of CaO, density of synthesized glass samples decreases significantly. Moreover, the Ca^{2+} ions are arbitrarily distributed in the glassy matrix. Hence, this leads to the creation of non-bonding oxygens (NBOs) which is attributed to an increase in the density of the fabricated glass samples but herein, the amount of CaO is decreasing as increasing the reinforcement of the CNTs. Therefore, density of the investigated glasses decreases with the rising content of CNT.

Density of the glasses against reinforcement concentration of CNT depicted in Figure 2 (a) while, the variation of molar volume, V_s increasing percentage of CNT and CaO are shown in Figure 2 (b) for all the fabricated glass samples in the glassy system SiO_2-Al_2O_3-MgO-K_2CO_3-CaO-MgF_2 (CNT 0.1-0.7). This Figure clearly shows that as the reinforcement content of CNT increases, the molar density decreases steadily up to a certain point i.e. CNT 0.4 (mol%) and further decreases gradually up to an extent.

3.3 Infrared spectroscopic study of the glasses

The infrared spectra of all synthesized glass samples GCNT0.1, GCNT 0.2, GCNT0.3, GCNT0.4, GCNT0.5 and GCNT0.7 are shown in Figure 3 (a-f) respectively. All the glass spectra exhibited eleven intense transmittance bands within the wavenumber range of 600 to 4000 cm^{-1}. For a particular peak corresponding to their different wavenumber starting from higher to lower wavenumber side including their respective band assignments are presented in Table 2. The first transmittance band lies in the wavenumber range from 3881-3820 cm^{-1} that is attributed to the O-H bonds of stretching vibrations as well as the H-O-H bending vibrations of the bonds [63]. Further, broad transmission bands were observed within the wavenumber range of 3600-3750 cm^{-1} which are assigned due to the O-H group vibrations [64-66]. However, the transmission bands in the wavenumber region from 2911-2925 cm^{-1} are owing to the growth of hydrogen bonding in the glassy matrix [67,68]. Two distinct peaks were also observed at 2920 and 2923 cm^{-1} which are assigned due to the formation of C-H stretching vibrations; probably originated from the surface of the CNT and nicely dispersed in a glassy matrix [69,70]. The broad transmission band 6 lies in the region from 2346 - 2354 cm^{-1} and recognized to the formation of O-H bond which probably due to the hygroscopic nature of K_2CO_3 and CaO. [67]. Moreover, all the O-H bonding groups observed at various wavenumbers that were formed at the non-bridging oxygen (NBO) sites in the glassy matrix [67]. Further, the transmission band lies in the wavenumber 1690-1697 cm^{-1} revealing the stretching vibrations of hydroxyl groups and the existence of water molecules [71]. However, the intense and sharp band lies within wavenumber range from 1525-1530 cm^{-1} which are attributed to the stretching vibrations of C=O group on the exterior surface of the CNT [69]. Additionally, as rising the reinforcement of CNT, the centers of the bands within their wavenumber

range are shifted towards low wavenumber side. It might be owing to the increase in the ratio of oxygen to CaO atoms that are associated with NBOs [72].

The observed bands in the region 1200-1250 cm^{-1} are attributed to the stretching vibrations of O-Si-O in the glassy network [73]. The various counts of NBO in the SiO_4 tetrahedral were observed due to the wavenumbers in the region 840-1250 cm^{-1} [74]. The band corresponds to the wavenumber 901 cm^{-1} representing the elongating vibrations of the $Al-O^-$ - alumina-silica-oxygen bridge [75-78]. However, the band noticed at 915 cm^{-1} revealed the vibrations of $Si-O^-$ [75,76]. A low intensity transmission band was also observed at ~840 cm^{-1} that assigned to the bending vibrations of H-Si-O [73]. Moreover, it is gradually lifted near to the higher wavenumber side as increasing the content of CNT. As the presence of Al in these glasses exist, a transmission band lies in the wavenumber range of 700 - 750 cm^{-1} and shows the tetrahedral coordinate of Al as center of gravity at ~695 cm^{-1} [79,80]. The formation of pseudo wollastonite confirmed the wavenumber 714 cm^{-1} [75]. The transmission band in the range 691-700 cm^{-1} corresponds to the bending vibrations Si-O-Al and Si-O-Si [79,81]. The transmission bands at 691 and 695 cm^{-1} are assigned to the symmetric stretching vibrations of Si-O-Si and vibrations of silico-rings in the glassy matrix [75,82,83]. The wide bands in the region 600-750 cm^{-1} are ascribed to the symmetric stretching vibrational modes of Si-O- (Si, Al) among the tetrahedral in the glassy matrix [84].

3.4 UV- Vis spectroscopic analysis

The UV-Vis absorption spectroscopy analysis helped to observe the absorption of UV radiation. The optical absorption spectra of all glass samples i.e. GCNT0.1, GCNT0.2, GCNT0.3, GCNT0.4, GCNT0.5 and GCNT0.7 along with Davis and Mott plots are shown in Figure 4 (a) & (b) respectively. From Figure 4 (a), it is noticed that merely a single transition has been observed within the wavelength region of ~285-350 nm which are denoted by two different dashed parallel

lines in their spectra. The calculated values of the band gap of each sample are given in Table 1. and these values were observed within the wavelength region of 200-1000 nm. The oxygen bonding strength is essential to calculate the distinct values of optical band gap in the glassy matrix [79]. As the reinforcement of CNT gradually increases from 0.1-0.7 and CaO decreases simultaneously, the values of band gap don't show any discrete sequence. The glass composition similar to this composition a slight change in the dopant content, change its optical band gap values from 3.59- 3.65 eV [79]. However, the observed band gap in the present glassy system SiO_2-Al_2O_3-MgO-K_2CO_3-CaO-MgF_2-CNT was found to be more i.e. 3.89- 4.34 eV as compared to the reported values [79]. As no sharp absorbance peak is observed in Figure 4 (a), it can be concluded that the glass samples are UV- inactive glasses due to a higher optical band gap.

3.5 Raman spectroscopic analysis

In order to give more insight into the structure of glasses, the Raman spectra of various bioactive glass samples GCNT0.1, GCNT 0.2, GCNT0.3, GCNT0.4, GCNT0.5 and GCNT0.7 were recorded and they containing seven contrast peaks in the range of 30 – 2000 cm^{-1}. All recorded spectra are shown in Figure 5 (a-f) respectively and their respective band assignments associated with their peak positions are enlisted in Table 3. The Raman bands in the region 1323-1326 cm^{-1} correspond to the occurrence of some defects in the CNT structures which are probably due to the melt-quenching during the synthesis of glasses [85]. However, the peaks occur in the range of 1200-1300 cm^{-1} (broad bands) are associated with the asymmetric vibrations of SiO_4 tetrahedral molecules [86,87]. The peak at 650 cm^{-1} is due to the bending vibrations and revealed the bridging oxygen (BO) of SiO_4 molecules [86,88]. The bands in the region of 600-700 cm^{-1} are assigned due to the bending or stretching vibrations of Si-O-Si bonds [89]. The bands at different wavenumbers i.e. 341, 344 and 348 cm^{-1} are assigned due to the mixed stretching and bending

vibrations of Si-O-Si bonds [86,90]. Further, the Raman bands reveal the wavenumbers 173, 178 and 180 cm^{-1} which are associated with the Si-O bonds of stretching vibrations [91]. An intense band at ~141 cm^{-1} is occurred due to the enlarging vibrations of O-H bond [92]. Hence, FTIR and Raman spectroscopic results revealed that glasses were formed through glass forming networks of silicate, alumina and network modifiers as cations of alkaline earth atoms. The silicate networks are modified by using several oxides such as Al_2O_3, MgO, K_2CO_3, CaO, MgF_2 in the glassy matrix.

3.6 Nuclear magnetic resonance (NMR) study

Solid State Nuclear Magnetic Resonance (SSNMR) spectroscopy is an indispensable microscopic tool to discriminate the same type of atoms in different chemical environments, because a characteristic frequency (Larmour frequency) of the NMR-active nucleus is different in different bonding environments. Hence, by utilizing this difference, it is possible to identify and quantify the number of nuclei present in different chemical environments. As long-range ordering is absent in glasses, so structural disorder within the glassy network can be identified by detecting the local bonding environment around the silicon nucleus. Different Q^n species ranging from $n = 0$ to $n = 4$ in silicate networks can be separated by measuring their isotropic chemical shifts [23-25,93,94].

Silicon is regarded as the archetypal glass former with a connected network of SiO_4 tetrahedra. The corner shearing oxygen atoms of the silicon network (Si-O-Si linkage) which are connected with two silicon are designated as bridging oxygen. When alkaline-earth cations (Mg^{2+}, Ca^{2+}) are added in the network, the silicon network is depolymerized. As a result, non-bridging oxygen (NBO) atoms are formed within the network, which is connected with one Si atom and another network modifier cation (say M) via Si-O-M linkage. So, the structural and local chemical environment within the silicate network is characterized by the presence of several kinds of Si-

environments denoted by $Q^{(0)}$, $Q^{(1)}$, $Q^{(2)}$, $Q^{(3)}$, and $Q^{(4)}$. The silicon tetrahedral without the presence of another tetrahedral silicon neighbor is denoted by $Q^{(0)}$. When one end of a silicon tetrahedral is connected with another silicon tetrahedral via an oxygen bridge, then it is denoted by $Q^{(1)}$. Whereas, Si-tetrahedral connected with two and three neighboring silicon tetrahedral via oxygen are designated as $Q^{(2)}$ and $Q^{(3)}$ respectively. When all four corners oxygen atoms of the silicon tetrahedral are shared by the other four adjacent silicon tetrahedral, then this type of fully cross-linked framework is designated as $Q^{(4)}$ species of silicon network. The model of silicon-network within the glass compound can be determined by statistically random distribution. For any given molar concentration of cations, the probability of having different Q^n species is determined by the constraints of charge and mass balance.

Figure 6 (a-e) shows ^{29}Si MAS SSNMR spectra of glass system SiO_2-Al_2O_3-MgO-K_2CO_3-CaO-MgF_2-CNT with a different fraction of CNT as 0.1 (referred as GCNT0.1), 0.3 (referred as GCNT0.3), 0.4 (referred to as GCNT0.4), 0.5 (referred to as GCNT0.5) and 0.7 (referred to as GCNT0.7). The ^{29}Si MAS SSNMR spectra of five samples were fitted by using nonlinear least-square spectral fitting by using *dmfit software* [95], where the mean position of the Gaussian distribution for $Q^{(0)}$, $Q^{(1)}$, $Q^{(2)}$, $Q^{(3)}$, and $Q^{(4)}$ species were taken as -67.00ppm, -72.00 ppm, -80.20 ppm, -90.00 ppm and – 100.00 ppm respectively.

Silicate melts are formed by a silicate network which is associated with silicate tetrahedral that are connected with each other via oxygen bonds (Si-O-Si). As the cations are introduced into the glassy melts, its breakdowns Si-O-Si bonds and non-bridging oxygens (NBOs). Anionic equilibrium is sustained within silicate matrix by succeeding the equation among different $Q^{(n)}$ species [31, 96-100].

$$2Q^{(n)} \rightarrow Q^{(n-1)} + Q^{(n+1)} \quad (4)$$

And

$$2Q^{(0)} = 2Q^{(1)} + (O)^2 \quad (5)$$

Where $(O)^2$ represents oxygen, which is not assured by the silicon tetrahedra and these are referred as free-oxygen. However, the equilibrium constant is represented by the following equation:

$$K_n = \frac{[Q^{(n+1)}][Q^{(n-1)}]}{[Q^{(n)}]^2}, \text{ where } n = 3, 2, 1 \text{ k} \quad (6)$$

For $n = 3$, the equilibrium constant is

$$K_3 = \frac{[Q^{(4)}][Q^{(2)}]}{[Q^{(3)}]^2} \quad (7)$$

For $n = 2$, the equilibrium constant is

$$K_2 = \frac{[Q^{(3)}][Q^{(1)}]}{[Q^{(2)}]^2} \quad (8)$$

And for $n = 1$, the equilibrium constant is

$$K_1 = \frac{[Q^{(2)}][Q^{(0)}]}{[Q^{(1)}]^2} \quad (9)$$

Table 4. shows the values of K_1, K_2 and K_3 for different synthesized glass samples, which indicates the distribution of $Q^{(n)}$ species within the silicate-network is random [32,97,100,101]. Within the silicate network, Ca^{2+} and Mg^{2+} ions are randomly distributed. This leads to the generation of non-bonding oxygens within the network. As the ionic radius of Ca^{2+} ions (1.00-1.12 A^0) are much larger than Mg^{2+} ions (0.57-0.71 A^0), so it is expected that Ca-NBO and Mg-NBO coordination polyhedra are present in the glass-network. This type of random distribution of dissimilar Ca-NBO and Mg-NBO coordination polyhedral leads to the structural as well as topological frustration and this is the reason why the most random distribution of different $Q^{(n)}$ species are observed within the network [102]. This result supports the result of the infrared spectroscopic study.

3.7 Contact angle analysis

Contact angle study showed the hydrophilic nature and chemical diversity of the solid surface of CNT doped glass samples. It is reported in the literature that if the value of contact angle less than 90◦ then the material is hydrophilic while greater than 90◦, then the material nature is hydrophobic [103,104]. Hence, the hydrophilic nature of CNT doped glassy samples was determined using contact angle measurements. The glass sample GCNT0.1 reveals less contact angle, 18.14º that is advantageous for hydrophilic nature of glassy materials whereas glass sample GCNT0.7 (0.7 % of CNT) shows hydrophobic nature [105]. The contact angle of the all synthesized bioactive glasses GCNT0.1, GCNT0.3, GCNT0.4, GCNT0.5 and GCNT0.7 were calculated and depicted in Figure 7 (a-f) respectively. Moreover, the calculated values of contact angles are determined by using 'ImageJ' software and are enlisted in Table 1. From Table 1, it is clearly noticed that among the all values of contact angle, the glass sample GCNT0.1, exhibited the lowest value i.e. 18.14º, while it is found to be maximum, 77.8° for GCNT0.7 containing large doping concentration of CNT. High value of contact angle is obtained at 77.8° for GCNT0.7 including the highest value of density, 2.98 gm/cc.

As increasing doping concentration of CNT, the contact angle has to be increased up to 77.8° which is responsible to a decrease in hydrophilic nature by the creation of hydrophobic layers on the surface of these bioactive glass samples. The variation of contact angle with increasing doping percentage of carbon nano tube is revealed in Figure 7 (g). Consequently, it reveals that the value of contact angle is directly proportional to the increasing doping percentage of CNT. Additionally, the hydrophilic behavior is mainly owing to the tiny pores and rough surface of the glass sample which is attributed for the lowest density of the GCNT0.1. Therefore, the lowest value of density and contact angle may offer the transportation of the body fluid and probably

enhance the tissue regeneration on the surface of this synthesized bioactive glass sample GCNT0.1 [106].

3.8 Mechanical properties of the glasses

The study of mechanical properties with various parameters such as storage modulus, length, stiffness, and loss modulus were plotted against strain for different glass samples i.e. GCNT0.1, GCNT0.3 and GCNT0.7 and shown in Figure 8 (a-c). The three parameters i.e. loss modulus, storage modulus and stiffness in the three glass samples GCNT0.1, GCNT0.3 and GCNT0.7 are found to be increased with an increase in strain and the length parameter decreases simultaneously. The same trend has been observed in all three glass samples. The maximum values of storage modulus, loss modulus, and stiffness are 5058.959×10^4 kPa, 5058.9590×10^4 kPa and 10000×10^6 N/m respectively for the glass sample GCNT0.7.

Herein, the higher value of storage modulus is a signature by the glass sample to store deformation energy in an elastic limit which is directly associated to the extent of cross-linking within the glassy matrix. Moreover, the higher degree of cross-linking the greater the storage modulus. So, it is concluded that as increasing the content of CNT the mechanical strength and resists deformation in response to an applied force of this glass sample object is enhanced significantly.

3.9 Surface morphological analysis

The SEM images of various bioactive powdered glass samples GCNT0.1, GCNT0.3, GCNT0.4, GCNT0.5, and GCNT0.7 are shown in Figure 9 (a-e) respectively. Figure 9 (a) depicts the randomly oriented irregular shaped fine particles (100 nm) of the synthesized glass sample. These fine particles are well interrelated to each other and appearing similar to a layered material. Further as increasing the doping amount from 0.1 to 0.2 the morphology of the glass particle was

completely changed including their shape and size (Figure 9 b and c). The presence of the tiny CNT was clearly observed in these SEM images. Moreover, as increasing the doping concentration of CNT in these glassy compositions, the various CNT can be seen easily. The magnified portion of the SEM images are shown as the insets of Figure 9 (d and e). The average length to diameter ratio was found to be the order of ~450 to ~50 nm. The CNTs are well dispersed into the glassy matrix and their shape and size are probably enhanced in comparison to their original shape and size. The enhancement in their size might be owing to the dispersion in the glassy matrix during the synthesis of the glasses. It has already been reported by Aria et al. that as-grown CNT are hydrophobic in nature, and they become more super hydrophobic when passing through vacuum pyrolysis treatment [107]. Therefore, the minor reinforcement of CNT into a glassy matrix can tune the hydrophobicity significantly.

4 Biological Activities

4.1 Effect of GCNT0.1 and GCNT0.7 on cell viability

Further, in order to check the effect of GCNT0.1 and GCNT0.7 on the cell viability of ROB cells, MTT assay was carried to analyze in-vitro cytotoxicity of these synthesized bioactive glass samples. Herein, the cell viability is denoted in terms of absorbance at 570 nm. MTT reagent was added to the ROB cells treated with five different concentrations, 0.01, 0.1, 1.0, 10 and 100 μg/ml of the samples GCNT0.1 and GCNT0.7 (Figure 10 a & b). The first three concentrations, 0.01, 0.1, and 1.0 μg/ml treatment of GCNT0.1 were the concentrations that exhibiting substantial cell proliferation. Nevertheless, the sample GCNT0.7 displayed admirable cell viability at 0.1 μg/ml. Moreover, as the glass sample concentration was augmented, the cell viability repeatedly decreased in comparison to the control. So, based on these results, the glass sample GCNT0.7 was found to be better than sample GCNT0.1. Hence, these outcomes verify that the fabricated glass

sample GCNT0.7, reinforced with 0.7 % CNT is highly biocompatible, nontoxic in nature, and can be used for various potential biomedical applications.

4.2 Effect of GCNT0.1 and GCNT0.7 on osteoblast differentiation

For investigating osteogenic potential of the bioactive glass samples GCNT0.1 and GCNT0.7, ALP assay was carried out where the production of alkaline phosphatase serves as a marker of osteoblast differentiation. Figure 10 (c and d) depicts the ALP activity of ROB cells treated with glass samples GCNT0.1 and GCNT0.7. From Figure 10 c, it has been clearly observed that the ALP activity was found to be maximum at 0.01 μg/ml and thereafter decreased gradually up to 10 μg/ml. However, ROB cells upon treatment of the sample GCNT0.7, at concentrations from 0.01 μg/ml to 100 μg/ml significantly increases the production of ALP enzyme as compared to control ROB cells where no treatment was given (Figure 10 d). Thus, it indicates that GCNT0.7 increased the differentiation of ROB cells at all concentrations whereas glass sample GCNT0.1 having the least concentration of CNT doesn't show significant osteoblast differentiation. Hence, based on the ALP study, the fabricated glass sample GCNT0.7 may be a potential bioactive glassy material for bone implant applications. Henceforth, the ALP as well as cell viability consequences are in good promise with each other. Besides, this study reveals that 10 and 100 μg/ml treatment of GCNT0.7 is the best bioactive glassy material which might be used for further biological studies such as in-vivo and their applications. Consequently, based on spectroscopic, microstructural, mechanical, and biological outcomes, the fabricated glass sample GCNT0.7 can be used for a biomedical application like bone/dental implants.

4.3 Effect of saline fluid, distilled water and hydrochloric acid

Further, substantial characteristics of the synthesized glass samples were studied to validate the stability in saline fluid, distilled water and HCL acid respectively. The variation of weight loss

in saline water against increasing weight percentage of CNT of the glasses GCNT0.1, GCNT0.3, GCNT0.4, GCNT0.5, and GCNT0.7 are shown in Figure 11 (a). Almost constant weight loss for the glass samples GCNT0.1, GCNT0.3, GCNT0.4, was observed and then it was found to be decreased as increasing the concentration of CNT (Figure 11). The absorption of saline fluid results exhibited that the synthesized glass samples, GCNT0.5 and GCNT0.7 (large concentration of CNT) were found to be very stable (weight loss 0.0004 gm) in comparison to the glass samples GCNT0.1, GCNT0.3, and GCNT0.4 (0.0005 gm), even not displaying any significant degradation after 8 h treatment. This is due to the large concentration of CNT in these glasses. Moreover, the large stability of CNT in saline water is attributed to an extremely high salt rejection capability [108]. The variation of weight loss in distilled water of the glass samples GCNT0.1, GCNT0.3, GCNT0.4, GCNT0.5, and GCNT0.7 are shown in Figure 11 (b), which are quite negligible i.e. 0.0004, 0.0003, 0.0002, 0.0001 and 0.0001 gm respectively. The samples were immersed in distilled water for the duration of 8 h. Apparently, major weight loss was not observed which concludes that glass samples are highly insoluble in the distilled water. The discrepancy of the glass samples GCNT0.1, GCNT0.3, GCNT0.4, GCNT0.5, and GCNT0.7 in HCL solution with 60% HCL, 40% HCL, 20% HCL, and 10% HCL respectively for the duration of 3 h are shown in Figure 11 (c). The weight loss is observed maximum in GCNT0.1 in 60% HCL solution i.e. 0.1601 mg and minimum in GCNT0.7 in 10% HCL solution i.e. 0.0362 mg. The weight loss increases with the increment of the concentration of acid along with the addition in the amount of CNT. This analysis implies that the stability of glass samples was found to be greatest for GCNT0.7 in 10% HCL solution.

5 Conclusions

In summary, bulk transparent bioactive glasses were prepared via conventional melt quenching method. XRD analysis revealed the unstructured behavior of these glasses. The experimental study demonstrated that the structural, morphological, mechanical and biological properties strongly depend on the chemical composition of these synthesized bioactive glass samples. FTIR results showed the presence of wide bands near the low wavenumber side and demonstrating that the fabricated glasses are more effective in comparison to the lower wavenumber. Moreover, stretching vibrations occur in the range of 850-990 cm^{-1} which are due to the formation of SiO_4 tetrahedron with various number of BO atoms whereas the band in the region 500–700 cm^{-1} attributed to bending vibrations of Si–O–Si and Si–O–Al linkages. ^{29}Si-MAS-NMR measurement reveals that the random distribution of two dissimilar cations Ca^{2+} and Mg^{2+} within the silicate network leads to structural and topological frustration. Less concentration of CNT reinforced glass sample exhibited the lowest value of contact angle 18.14^o, while it is exhibited a maximum, 77.8° for the highest concentration of CNT reinforced glass sample. The biological activities of glass sample GCNT0.7 revealed good cell viability, improved differentiation of osteoblast cells and adequate stability in saline water. Therefore, this glass sample GCNT0.7 can be used for various biomedical applications. Furthermore, these outcomes may feat the probabilities for application in dentistry and orthopedics. Hence, the current study is of great prominence for developing a new class of glassy material and outspreading their potential biomedical multifunctional applications.

Acknowledgements

Dr. C. R. Gautam is very grateful to UGC, New Delhi, India for providing the financial support under UGC Research Award No. F. 30-33/2011 (S.A.). Dr. Manasi Ghosh is indebted to Science and Engineering Research Board (SERB), Department of Science and Technology (DST),

government of India (File no. EMR/2016/000249) and UGC-BSR (File no.30-12/2014BSR) for financial support. And we are also thankful to Sophisticated Instrumentation Centre (SIC) of Dr. Hari Singh Gour Central University for extending the solid-state NMR facility.

References

[1] Nan Y, Lee WE, James PF. Crystallization behavior of $CaO-P_2O_5$ glass with TiO_2, SiO_2 and Al_2O_3 additions. *J Am Ceram Soc* 1992, **75**: 1641-1647.

[2] Kokubo T, Matsushita T, Takadama H. Titania-based bioactive materials. *J Eur Ceram Soc* 2007, **27**: 1553-1558.

[3] Liping Y, Xiao H, Cheng Y. Influence of magnesia on the structure and properties of $MgO-Al_2O_3-SiO_2-F^-$ glass-ceramics. *Ceram Int* 2008, **34**: 63-68.

[4] Hench LL, Splinter RJ, Allen WC, et al. Bonding mechanisms at the interface of ceramic prosthetic materials. *J Biomed Mater Res* 1971, **5**: 117-141.

[5] Cheng Y, Xiao H, Shuguang C, et al. Structure and crystallization of B_2O_3 $Al_2O_3-SiO_2$ glass. *Phys B* 2009, **404**: 1230-1234.

[6] Tommila M, Jokinen J, Wilson T, et al. Bioactive glass-derived hydroxyapatite-coating promotes granulation tissue growth in subcutaneous cellulose implants in rats. *Acta Biomater* 2008, **4**: 354-361.

[7] Matsumoto T, Kuroda R, Mifune Y, et al. Circulating endothelial/skeletal progenitor cells for bone regeneration and healing. *Bone* 2008, **43**: 434-439.

[8] Yang Q, Sui G, Shi YZ, et al. Osteocompatibility characterization of polyacrylonitrile carbon nanofibers containing bioactive glass nanoparticles. *Carbon* 2013, **56**: 288-295.

[9] Wilson J, Piggott GH, Schoen FJ, et al. Toxicology and biocompatibility of bioglasses. *J Biomed Mater Res* 1981, **15**: 805-817.

[10] Vogel W, Höland W, Naumann K, et al. Development of machineable bioactive glass ceramics for medical uses. *J Non-Cryst Solids* 1986, **80**: 34-51.

[11] Hench LL. Bioceramics: from concept to clinic. *J Am Ceram Soc* 1991, **74**: 1487-1510.

[12] Stoor P, Kirstilä V, Söderling E, et al. Interactions between bioactive glass and periodontal pathogens. *Microb Ecol Health Dis* 1996, **9**: 109-114.

[13] El-Kady AM, Ali AF, Rizk RA, et al. Synthesis, characterization and microbiological response of silver doped bioactive glass nanoparticles. *Ceram Int* 2012, **38**: 177-188.

[14] Shih SJ, Chen CY, Lin YC, et al. Investigation of bioactive and antibacterial effects of graphene oxide-doped bioactive glass. *Adv Powder Technol* 2016, **27**: 1013-1020.

[15] Shih SJ, Hong BJ, Lin YC. Novel graphene oxide-containing antibacterial mesoporous bioactive glass. *Ceram Int* 2017, **43**: S784-S788.

[16] Jones JR. Reprint of: review of bioactive glass: from Hench to hybrids. *Acta Biomater* 2015, **23**: S53-S82.

[17] Hench LL, Paschall HA. Direct chemical bond of bioactive glass-ceramic materials to bone and muscle. *J Biomed Mater Res* 1973, **7**: 25-42.

[18] Jones JR, Brauer DS, Hupa L, et al. Bioglass and bioactive glasses and their impact on healthcare. *Int J Appl Glass Sci* 2016, **7**: 423-434.

[19] Baino F, Novajra G, Miguez-pacheco V, et al. Bioactive glasses: Special applications outside the skeletal system. *J Non-Cryst Solids* 2016, **432**: 15-30.

[20] Wallace KE, Hill RG, Pembroke JT, et al. Influence of sodium oxide content on bioactive glass properties. *J Mater Sci Mater Med* 1999, **10**: 697-701.

[21] Kansal I, Reddy A, Muñoz F, et al. Structure, biodegradation behavior and cytotoxicity of alkali-containing alkaline-earth phosphosilicate glasses. *Mater Sci Eng C* 2014, **44**: 159-165.

[22] Fiedler T, Videira AC, Bártolo P, et al. On the mechanical properties of PLC–bioactive glass scaffolds fabricated via BioExtrusion. *Mater Sci Eng C* 2015, **57**: 288-293.

[23] Janes N, Oldfield E. Prediction of silicon-29 nuclear magnetic resonance chemical shifts using a group electronegativity approach: applications to silicate and aluminosilicate structures. *J Am Chem Soc* 1985, **107**: 6769-6775.

[24] Martineau C, Michaelis VK, Schiller S, et al. Liquid-liquid phase separation in model nuclear waste glasses: A solid state double resonance NMR study. *Chem Mater* 2010, **22**: 4896-4903.

[25] Greaves GN, Gurman SJ, Catlow CRA, et al. A structural basis for ionic diffusion in oxide glasses. *Philo Mag A* 1991, **64**: 1059-1072.

[26] Day DE, White JE, Brown RF, et al. Transformation of borate glasses into biologically useful materials. *Glass Technol Part A* 2003, **44**: 75-81.

[27] Day DE, Erbe EM, Richard M, et al. Bioactive materials. US Patent No. 6709 744, 2004.

[28] Han X, Day DE. Reaction of sodium calcium borate glasses to form hydroxyapatite. *J Mater Sci Mater Med* 2007, **18**: 1837-1847.

[29] Zhao D, Huang W, Rahaman MN, et al. Mechanism for converting Al_2O_3-containing borate glass to hydroxyapatite in aqueous phosphate solution. *Acta Biomater* 2009, **5**: 1265-1273.

[30] Pan HB, Zhao XL, Zhang X, et al. Strontium borate glass: potential biomaterial for bone regeneration. *J Roy Soc Interface* 2010, **7**: 1025-1031.

[31] Sen S, Maekawa H, Papatheodorou GN. Short-range structure of invert glasses along the psudo-binary join $MgSiO_3$-Mg_2SiO_4: Results from 29Si and 25Mg MAS NMR spectroscopy. *J Phys Chem B* 2009, **113**: 15243-15248.

[32] Dorfeld WG. Structural thermodynamics of alkali silicates glasses. *Phys Chem Solids* 1988, **29**: 179-186.

[33] Li H, You DQ, Zhou CR, et al. Study on machinable glass-ceramic containing fluorophlogopite for dental CAD/CAM system. *J Mater Sci: Mater Med* 2006, **17**: 1133-1137.

[34] Shi D, Xuejun W. Bioactive ceramics: Structure, synthesis and mechanical properties. In Introduction to Biomaterials. Shi D, Ed. Beijing: Tsinghua University Press, 2006: 13-28.

[35] White AA, Best SM, Kinloch IA. Hydroxyapatite–Carbon Nanotube Composites for Biomedical Applications: A Review. *Int J Appl Ceram Technol* 2007, **4**: 1-13.

[36] Hench LL, Wilson J. Introduction. In An Introduction to Bioceramics. Hench LL, Wilson J, Eds. Singapore: World Scientific, 1993: 1-24.

[37] Bhong SY, More N, Choppadandi M, et al. Review on carbon nanomaterials as typical candidates for orthopaedic coatings. *SN Applied Sciences* 2019, **76**: 1-16.

[38] Habisreutinger SN, Nicholas RJ, Snaith HJ. Carbon nanotubes in perovskite solar cells. *Adv Energy Mater* 2017, **7**: 1601839-1601845.

[39] Iijima S. Carbon nanotubes: past, present and future. *Physica B* 2002, **323**: 1-5.

[40] Meng D, Rath SN, Mordan N, et al. In vitro evaluation of 45S5 Bioglass VR -derived glass-ceramic scaffolds coated with carbon nanotubes. *J Biomed Mater Res Part A* 2011, **99**: 435-444.

[41] Allen MJ, Tung VC, Kaner RB. Honeycomb carbon: a review of graphene. *Chem Rev* 2009, **110**: 132-145.

[42] Fonseca-Garcia A, Mota-Morales JD, Quintero-Ortega IA, et al. Effect of doping in carbon nanotubes on the viability of biomimetic chitosan-carbon nanotubes-hydroxyapatite scaffolds. *J Biomed Mater Res Part A* 2013, **102**: 3341-3351.

[43] Damaraju SM, Shen Y, Elele E, et al. Three-dimensional piezoelectric fibrous scaffolds selectively promote mesenchymal stem cell differentiation. *Biomaterials* 2017, **149**: 51-62.

[44] Muhulet A, Miculescu F, Voicu SI, et al. Fundamentals and scopes of doped carbon nanotubes towards energy and biosensing applications. *Mater Today Energy* 2018, **9**: 154-186.

[45] Yang L, Zhang L, Webster TJ. Carbon nanostructures for orthopedic medical applications. *Nanomedicine* 2011, **6**: 1231-1244.

[46] Meng YH, Tang CY, Tsui CP, et al. Fabrication and characterization of HA-ZrO_2-MWCNT ceramic composites. *J Compos Mater* 2010, **44**: 871-882.

[47] Meng DC, Ioannou J, Boccaccini AR. Bioglass-based scaffolds with carbon nanotube coating for bone tissue engineering. *J Mater Sci-Mater M* 2009, **20**: 2139-2144.

[48] Boccaccini AR, Chicatun F, Cho J, et al. Carbon nanotube coatings on bioglass-based tissue engineering scaffolds. *Adv Funct Mater* 2007, **17**: 2815-2822.

[49] Armentano I, Alvarez-Perez MM, Carmona- Rodriguez B, et al. Analysis of the biomineralization process on SWNT-COOH and F-SWNT films. *Mat Sci Eng C-Bio S* 2008, **28**: 1522-1529.

[50] Zanello LP, Zhao B, Hu H, et al. Bone cell proliferation on carbon nanotubes. *Nano Lett* 2006, **6**: 562-567.

[51] Khang D, Park GE, Webster TJ. Enhanced chondrocyte densities on carbon nanotube composites: The combined role of nanosurface roughness and electrical stimulation. *J Biomed Mater Res A* 2008, **86**: 253-260.

[52] Xiao Y, Gong T, Zhou S. The functionalization of multi-walled carbon nanotubes by in situ deposition of hydroxyapatite. *Biomaterials* 2010, **31**: 5182-5190.

[53] Guo YP, Yao YB, Ning CQ, et al. Fabrication of mesoporous carbonated hydroxyapatite/carbon nanotube composite coatings by microwave irradiation method. *Mater Lett* 2011, **65**: 1007-1009.

[54] Grossman DG. Tetrasilicic mica Glass-ceramics. Patent No – 3839005, 1974.

[55] Gautam CR, Manpoong CW, Gautam SS, et al. Synthesis, microstructure and dielectric properties of (Sr, Bi) TiO_3 borosilicate glass-ceramics. *J Ceram Sci Tech* 2016, **7**: 79-86.

[56] Gautam CR, Das S, Gautam SS, et al. Processing and optical characterization of lead calcium titanate borosilicate glass doped with germanium. *J Phys Chem Solids* 2018, **115**: 180-186.

[57] Arshad SE, Lee WE, James PF. Crystallization and microstructural evolution of commercial fluosilicate glass-ceramic. *Glass Technol* 2002, **43C**: 69-80.

[58] Yadav AK, Gautam CR. Synthesis, structural and optical studies of barium strontium titanate borosilicate glasses doped with ferric oxide. *Spect Lett* 2015, **48**: 514-520.

[59] Lamour G, Journiac N, Soues S, et al. Influence of surface energy distribution on neuritogenesis. *Colloids Surf B* 2009, **72**: 208–18.

[60] Ahamad MI, Prakash R, John AA, et al. Induced osteoblast differentiation by amide derivatives of stilbene: The possible osteogenic agents. *Bioorg Med Chem Lett* 2020, **30**: 127138-127144.

[61] Dixit M, Raghuvanshi A, Gupta CP, et al. Medicarpin, a natural pterocarpan, heals cortical bone defect by activation of notch and Wnt canonical signaling pathways. *PLoS One* 2015, **10**: e0144541-e0144556.

[62] Prakash R, John AA, Singh D. miR-409-5p negatively regulates Wnt/Beta catenin signaling pathway by targeting Lrp-8. *J Cell Physiol* 2019, **234**: 23507-23517.

[63] Venyaminov SY, Prendergast FG. Water (H_2O and D_2O) molar absorptivity in the 1000–4000 cm^{-1} range and quantitative infrared spectroscopy of aqueous solutions. *Anal Biochem* 1997, **248**: 234-245.

[64] Gautam CR, Yadav AK, Singh AK. A review on infrared spectroscopy of borate glasses with effects of different additives. *ISRN Ceramics* 2012, **2012**: 1-17.

[65] Adams RV, Douglas RW. Infra-red studies on various samples of fused silica with special reference to the bands due to water. *JSGT* 1959, **43**: 147-158.

[66] Scholzelt H. Glass: Nature, Structure and Properties. New York (USA): Springer, 1991.

[67] Gautam CR, Yadav AK, Mishra VK, et al. Synthesis, IR and raman spectroscopic studies of (Ba,Sr)TiO_3 borosilicate glasses with addition of La_2O_3. *OJINM* 2012, **2**: 47-54.

[68] Venktaraman A, Hiremath VA, Date SK, et al. A new combustion route to γ-Fe_2O_3 synthesis. *Bull Mater Sci* 2001, **24**: 617-621.

[69] Gupta VK, Agarwal S, Saleh TA. Synthesis and characterization of alumina-coated carbon nanotubes and their application for lead removal. *J Hazard Mater* 2011, **185**: 17-23.

[70] Hayati B, Maleki A, Najafi F, et al. Heavy metal adsorption using PAMAM/CNT nanocomposite from aqueous solution in batch and continuous fixed bed systems. *Chem Eng J* 2018, **346**: 258-270.

[71] Kumar V, Arora N, Pandey OP, et al. FTIR and optical assessment of zinc doped calcium phospho-borosilicate sol-gel glasses/glass-ceramics. *AIP Conf Proc* 2015, **1675**: 030061-030065.

[72] Das S, Madheshiya A, Gautam SS, et al. Fabrication and optical characterizations of lead calcium titanate borosilicate glasses. *J Non-Cryst Solids* 2017, **478**: 16-22.

[73] Liu C, Qi Q, Seregin DS, et al. Effect of terminal methyl groups concentration on properties of organosilicate glass low dielectric constant films. *Jpn J Appl Phys* 2018, **57**: 07MC01-07MC07.

[74] Krishnan ML, Neethish MM, Ravi Kanth Kumar VV. Structural and optical studies of rare earth-free bismuth silicate glasses for white light generation. *J Lumin* 2018, **201**: 442-450.

[75] Partyka J, Leśniak M. Raman and infrared spectroscopy study on structure and microstructure of glass–ceramic materials from SiO_2–Al_2O_3–Na_2O–K_2O–CaO system modified by variable molar ratio of SiO_2/Al_2O_3. *Spectrochim Acta A Mol Biomol Spectrosc* 2016, **152**: 82-91.

[76] Sitarz M. The structure of simple silicate glasses in the light of middle infrared spectroscopy studies. *J Non-Cryst Solids* 2011, **357**: 1603-1608.

[77] Mozgawa W, Sitarz M, Rokita M. Spectroscopic study of different aluminosilicate structures. *J Mol Struct* 1999, **511-512**: 251-257.

[78] Mozgawa W, Sitarz M. Vibrational spectra of aluminosilicate ring strictures. *J Mol Struct* 2002, **614**: 273-279.

[79] Gautam CR. Synthesis and optical properties of SiO_2- Al_2O_3- MgO- K_2CO_3- CaO- MgF_2- La_2O_3 glasses. *Bull Mater Sci* 2016, **39**: 677-682.

[80] Pascual MJ, Duran A, Prado MO. A new method for determining fixed viscosity points of glasses. *Phys Chem Glasses* 2005, **46**: 512-520.

[81] Sharma SK, Yoder Jr HS, Matson DW. Raman study of some melilites in crystalline and glassy states. *Geochim Cosmochim Acta* 1988, **52**: 1961-1967.

[82] Sitarz M, Mozgawa W, Handke M. Vibrational spectra of complex ring silicate anions-method of recognition. *J Mol Struct* 1997, **404**: 193-197.

[83] Garai M, Sasmal N, Molla AR, et al. Effects of nucleating agents on crystallization and microstructure of fluorophlogopite mica-containing glass–ceramics. *J Mater Sci* 2014, **49**: 1612-1623.

[84] Zheng Q, Liu Y, Li M, et al. Crystallization behavior and IR structure of yttrium aluminosilicate glasses. *J Eur Ceram Soc* 2020, **40**: 463-471.

[85] Fesenko O, Dovbeshko G, Dementjev A, et al. Graphene-enhanced raman spectroscopy of thymine adsorbed on single-layer graphene. *Nanoscale Res Lett* 2015, **10**: 1-7.

[86] Yadav AK, Singh P. A review of structure of oxide glasses by raman spectroscopy. *RSC Advs* 2015, **5**: 67583-67609.

[87] Cheng K, Wan J, Liang K. Crystallization of R_2O–MgO–Al_2O_3–B_2O_3–SiO_2–F (R=K^+, Na^+) glasses with different fluorine source. *Mater Lett* 2001, **47**: 1-6.

[88] Petrescu S, Constantinescu M, Anghel EM, et al. Structural and physico-chemical characterization of some soda lime zinc alumino-silicate glasses. *J Non-Cryst Solids* 2012, **358**: 3280-3288.

[89] Huang F, Su H, Jing Y, et al. Microwave dielectric properties of glass-free $CaMg_{0.9-x}Li_{0.2}Zn_xSi_2O_6$ ceramics for LTCC applications. *Ceram Int* 2020, **46**: 18308-18314.

[90] Parkinson BG, Holland D, Smith ME, et al. Quantitative measurement of Q(3) species in silicate and borosilicate glasses using Raman spectroscopy. *J Non-Cryst Solids* 2008, **354**: 1936-1942.

[91] Saikia BJ, Parthasarathy G, Borah RR. Silicates in Kamargaon (L6) chondrite: A Raman spectroscopic study. *Open Acc J Math Theor Phy* 2018, **1**: 225-230.

[92] Tashiro K, Kobayashi M. Theoretical evaluation of three-dimensional elastic constants of native and regenerated celluloses: role of hydrogen bonds. *Polymer* 1991, **32**: 1516-1526.

[93] Smith KA, Kirkpatrick RJ, Oldfield E, et al. High resolution Si NMR spectroscopic study of rock forming silicates. *Am Min* 1983, **68**: 1206-1215.

[94] Ingram MD. Ionic conductivity and glass structure. *Philos Mag B* 1989, **60**: 729-740.

[95] Massiot D, Fayan F, Capron M, et al. Modelling one- and two-dimensional solid-state NMR spectra. *Magn Reson Chem* 2002, **40**: 70-76.

[96] Emerson JF, Stallworth PE, Bray PJ. High-field 29Si NMR studies of alkali silicate glasses. *J Non Cryst Solids* 1989, **113**: 253-259.

[97] Bray PJ. NMR studies of the structures of glasses. *J Non Cryst Solids* 1987, **95**: 45-60.

[98] Navrotsky A. Energetics of silicate melts. In Structure, Dynamics and Properties of Silicate Melts, Reviews in Mineralogy. Stebbins JF, McMillan PF, Dingwell DB, Eds. Washington (DC): Mineralogical Society of America, 1995: 121-143.

[99] Hess PC. Thermodynamic mixing properties and the structure of silicate melts. In Structure, Dynamics and Properties of Silicate Melts, Reviews in Mineralogy. Stebbins JF, McMillan PF, Dingwell DB, Eds. Washington (DC): Mineralogical Society of America, 1995: 145-190.

[100] Davis MC, Sanders KJ, Grandinetti PJ, et al. Structural investigations of magnesium silicate glasses by 29Si 2D Magic-Angle Flipping NMR. *J Non Cryst Solids* 2011, **357**: 2787-2795.

[101] Zhang P, Grandinetti PJ, Stebbins JF. Anionic species determination in $CaSiO_3$ glass using two-dimensional 29Si NMR. *J Phys Chem B* 1997, **101**: 4004-4008.

[102] Nasikas NK, Edwards TG, Sen S, et al. Structural Characteristics of Novel Ca-Mg orthosilicate and suborthosilicate glasses: results from 29Si and 17O NMR Spectroscopy. *J Phys Chem B* 2012, **116**: 2696-2702.

[103] Madheshiya A, Gautam CR, Kumar S. Synthesis, structural and X-ray absorption spectroscopy of $(Pb_xBi_{1-x})TiO_3$ borosilicate glass and glass ceramics. *J Asian Ceram Soc* 2017, **5**: 276-283.

[104] Yuan Y, Lee TR. Contact angle and wetting properties. In Springer Series in Surface Sciences. Bracco G, Holst B, Eds. Berlin: Springer, 2013: 3-34.

[105] Gautam CR, Kumar S, Biradar SK, et al. Synthesis and enhanced mechanical properties of MgO substituted hydroxyapatite: a bone substitute material. *RSC Adv* 2016, **6**: 67565-67574.

[106] Gautam CR, Gautam A, Mishra VK, et al. 3D interconnected architecture of h-BN reinforced ZrO_2 composites: structural evolution and enhanced mechanical properties for bone implant applications. *Ceram Int* 2019, **45**: 1037-1048.

[107] Aria AI, Gharib M. Reversible tuning of the wettability of carbon nanotube arrays: the effect of ultraviolet/ozone and vacuum pyrolysis treatments. *Langmuir* 2011, **27**: 9005-9011.

[108] Sahu P, Ali SM, Shenoy KT, et al. Nanoscopic insights of saline water in carbon nanotube appended filters using molecular dynamics simulations. *Phys Chem Chem Phys* 2019, **21**: 8529-8542.

Table 1 Glass sample code, nominal chemical composition of the glasses (mol %), density, molar volume, optical band gap and contact angle of the glass samples in the glassy system SiO_2-Al_2O_3-MgO-K_2CO_3-CaO-MgF_2-CNT

Glass sample code	Chemical composition of the glasses (mol %)						% of CNT	Density of glass samples (gm/cc)	Molar Volume (cm^3/mole)	Optical band gap (eV)	Contact Angle in degrees (^{0})
	SiO_2	Al_2O_3	MgO	K_2CO_3	CaO	MgF_2					
GCNT0.1	39	12	10	12	6.9	20	0.1	1.99±0.099	36.49±1.82	4.20	18.14
GCNT0.2	39	12	10	12	6.8	20	0.2	2.39±0.119	30.36±1.51	4.11	29.17
GCNT0.3	39	12	10	12	6.7	20	0.3	2.57±0.128	28.22±1.41	4.34	32.26
GCNT0.4	39	12	10	12	6.6	20	0.4	2.82±0.141	25.70±1.28	4.34	49.38
GCNT0.5	39	12	10	12	6.5	20	0.5	2.84±0.142	25.50±1.27	3.89	66.12
GCNT0.7	39	12	10	12	6.3	20	0.7	2.98±0.149	24.28±1.21	4.07	77.8

Table 2 Peak positions (cm^{-1}) and assignments of Fourier transform infrared spectra of investigated various glass samples in the glassy system SiO_2-Al_2O_3-MgO-K_2CO_3-CaO-MgF_2-CNT

Peak No.	Glass samples code						IR Band Assignments	Ref.
	GCNT0.1	GCNT0.2	GCNT0.3	GCNT0.4	GCNT0.5	GCNT0.7		
1a	3872	3838	3869	3881	3859	3840	Stretching vibrations of O-H bonds and bending vibrations of H-O-H bonds	[62]
b	3827		3828	3826	3834			
2	3743	3741	3743	3743	3742	3740	O-H group vibrations	[63-65]
3	3685	-	-	-	3681	3677	O-H group vibrations	[63-65]
4	3616	3615	3606	3612	3619	3618	O-H group vibrations	[63-65]
5	2911	2911	2920	2914	2923	2915	Hydrogen bonding and C-H stretching vibrations	[66-68]
6	2354	2347	2348	2350	2353	2350	O-H bonding	[66]
7	1695	1693	1694	1694	1697	1694	Stretching vibrations of hydroxyl group and water molecules	[70]
8	1527	1530	1525	1525	1530	1530	Stretching vibrations of C=O group on the surface of CNT	[68]
9	1225	1211	1207	1208	1207	1227	Stretching vibrations of O-Si-O	[72]
10	915	840	857	843	858	901	Stretching vibration of $Si\text{-}O^-/Al\text{-}O^-$	[74-77,73]
11	708	-	691	695	700	714	Symmetric stretching vibrations of Si-O- (Si, Al)	[83]

Table 3 Peak positions (cm^{-1}) and assignments of Raman spectra of investigated various glass samples in the glassy system SiO_2-Al_2O_3-MgO-K_2CO_3-CaO-MgF_2-CNT

Peak No.	Glass samples code						Raman band assignments	Ref.
	GCNT0.1	GCNT0.2	GCNT0.3	GCNT0.4	GCNT0.5	GCNT0.7		
1	1323	1326	1325	1324	1323	1324	Defects in the CNT structure	[84]
2	1258	1267	1263	1262	1261	1260	Asymmetric vibration of SiO_4	[85,86]
3	655	660	665	656	650	650	Bending and stretching vibrations of Si-O-Si	[88]
4	344	344	348	348	344	341	Mixed stretching and bending modes of Si-O-Si	[85,89]
5	178	180	173	173	178	178	Symmetric stretching vibrations of Si-O bonds	[90]
6	142	144	145	141	140	143	Stretching vibrations of O-H bonds	[91]

Table 4 Relative concentration (in %) of the Q^n species in SiO_2-Al_2O_3-MgO-K_2CO_3-CaO-MgF_2 with different fraction of CNT

Sample code	$Q^{(0)}$	$Q^{(1)}$	$Q^{(2)}$	$Q^{(3)}$	$Q^{(4)}$	K_1	K_2	K_3
GCNT0.1	7.91	8.12	26.72	48.95	8.29	3.20554	0.55672	0.09245
GCNT0.3	16.43	6.02	72.75	2.78	2.01	32.98204	0.00316	18.9208
GCNT0.4	23.00	8.12	62.65	5.24	1.05	21.8543	0.01084	2.39578
GCNT0.5	17.63	11.39	65.69	3.68	1.61	8.92697	0.00971	7.80961
GCNT0.7	16.45	15.73	60.36	5.63	1.82	4.01289	0.02431	3.4658

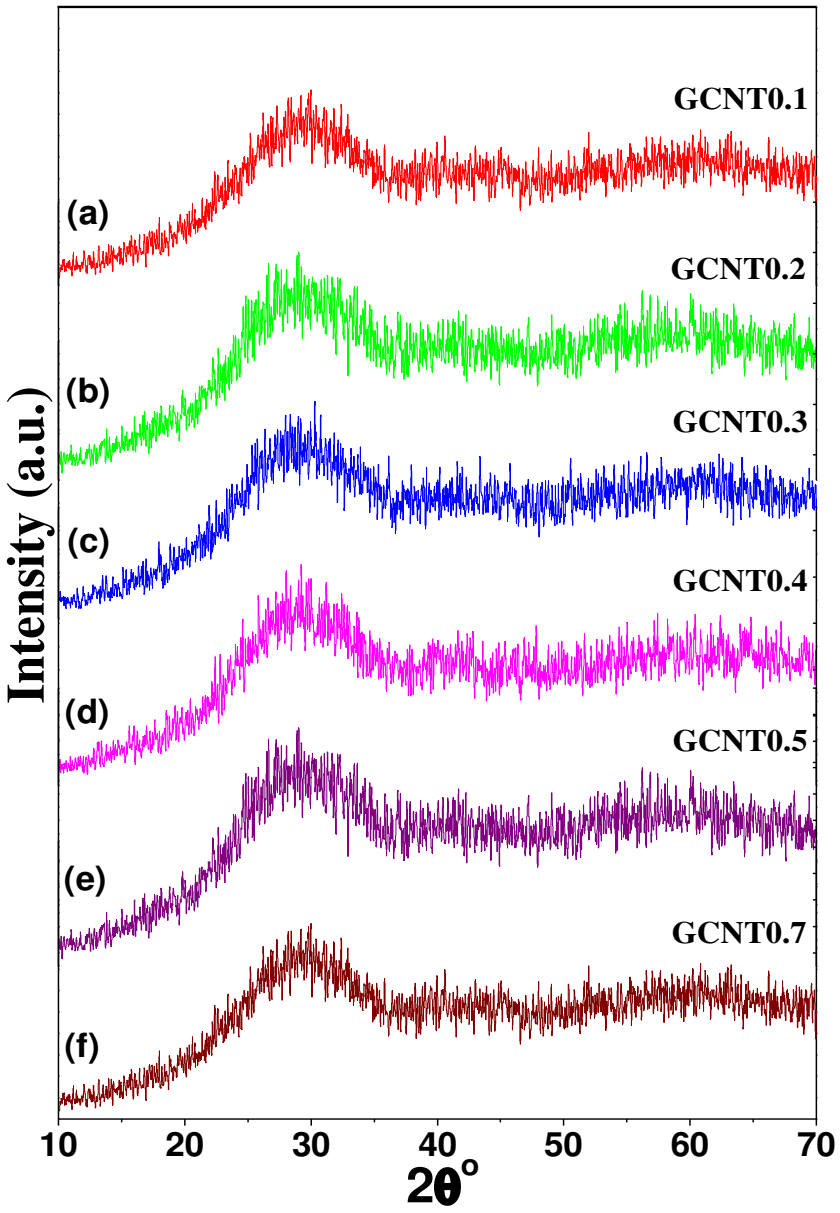

Fig. 1 XRD patterns of the glass samples (a) GCNT0.1, (b) GCNT0.2, (c) GCNT0.3, (d) GCNT0.4, (e) GCNT0.5 and (f) GCNT0.7 respectively.

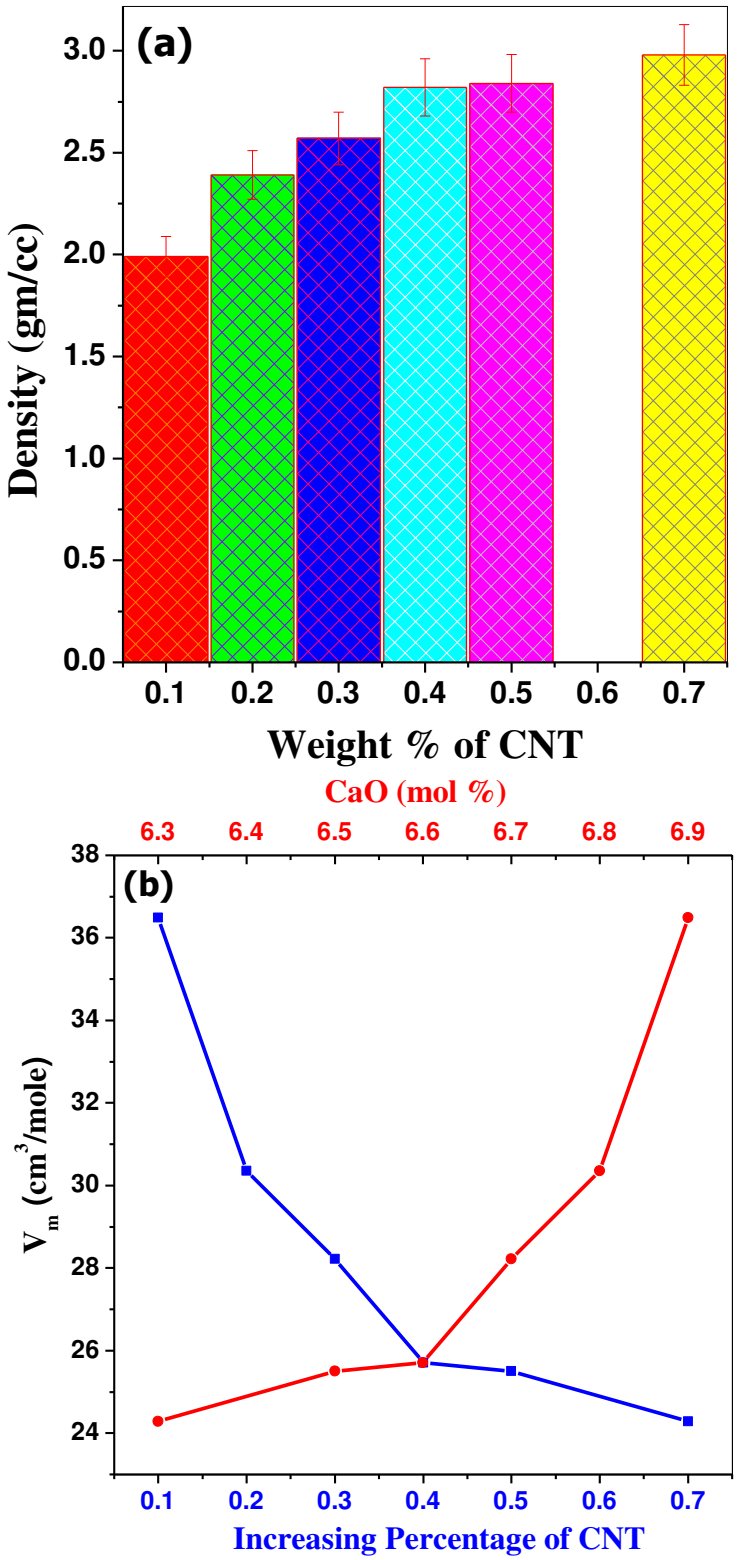

Fig. 2 (a) Density of glass samples Vs reinforcement concentration of CNT and (b) Variation of molar volume Vs percentage of CNT and CaO.

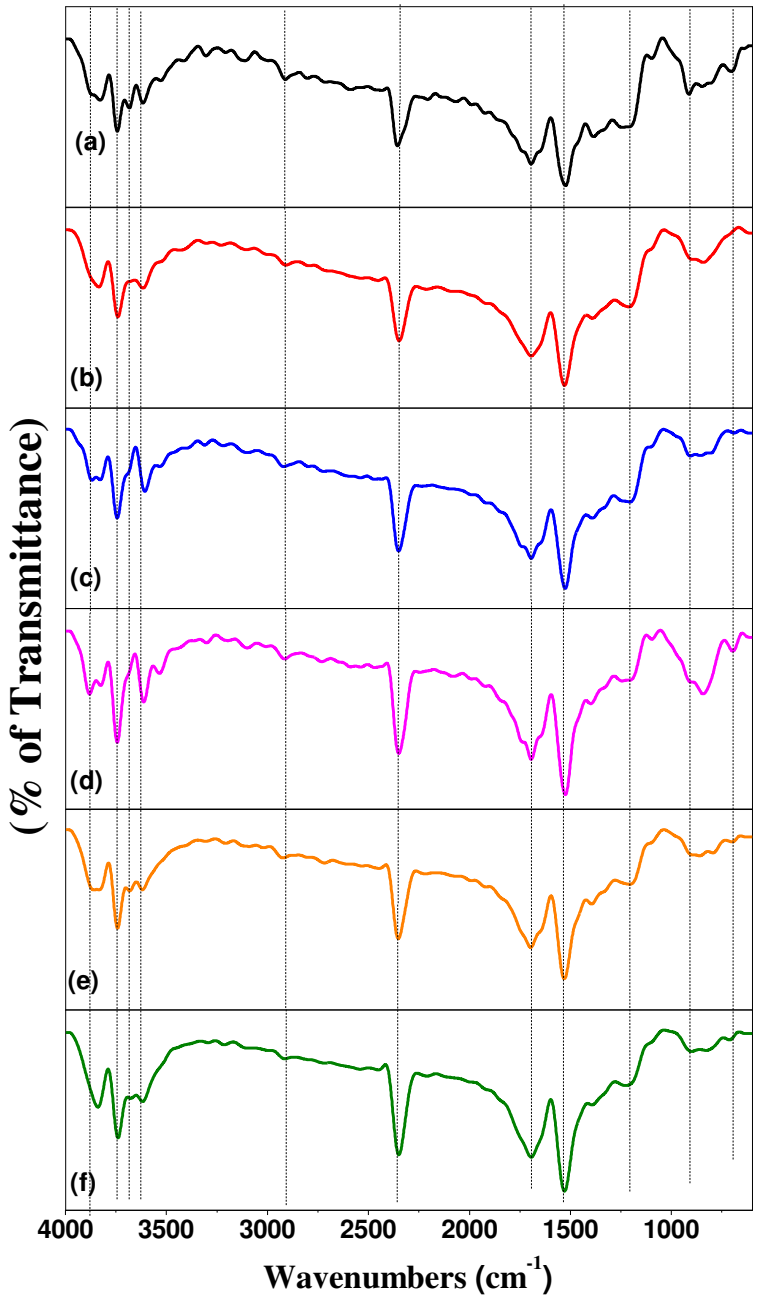

Fig. 3 IR patterns of glass samples (a) GCNT0.1, (b) GCNT0.2, (c) GCNT0.3, (d) GCNT0.4, (e) GCNT0.5 and (f) GCNT0.7 respectively.

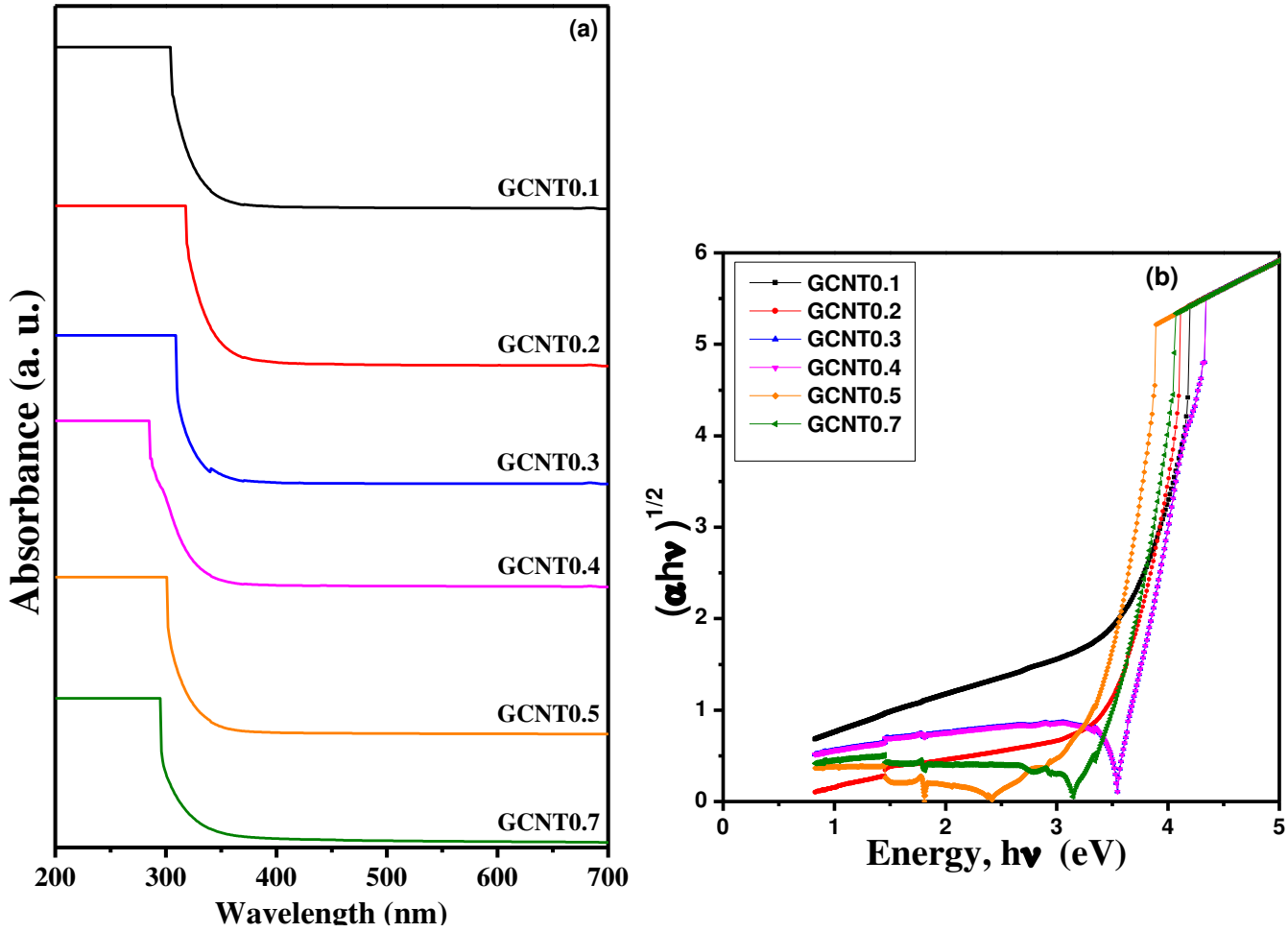

Fig. 4 (a) UV-Vis spectra of glass samples GCNT0.1, GCNT0.2, GCNT0.3, GCNT0.4, GCNT0.5 and GCNT0.7 and (b) Davis and Mott plots of $(\alpha h\nu)^{1/2}$ versus hν of glass samples GCNT0.1, GCNT0.2, GCNT0.3, GCNT0.4, GCNT0.5 and GCNT0.7 respectively.

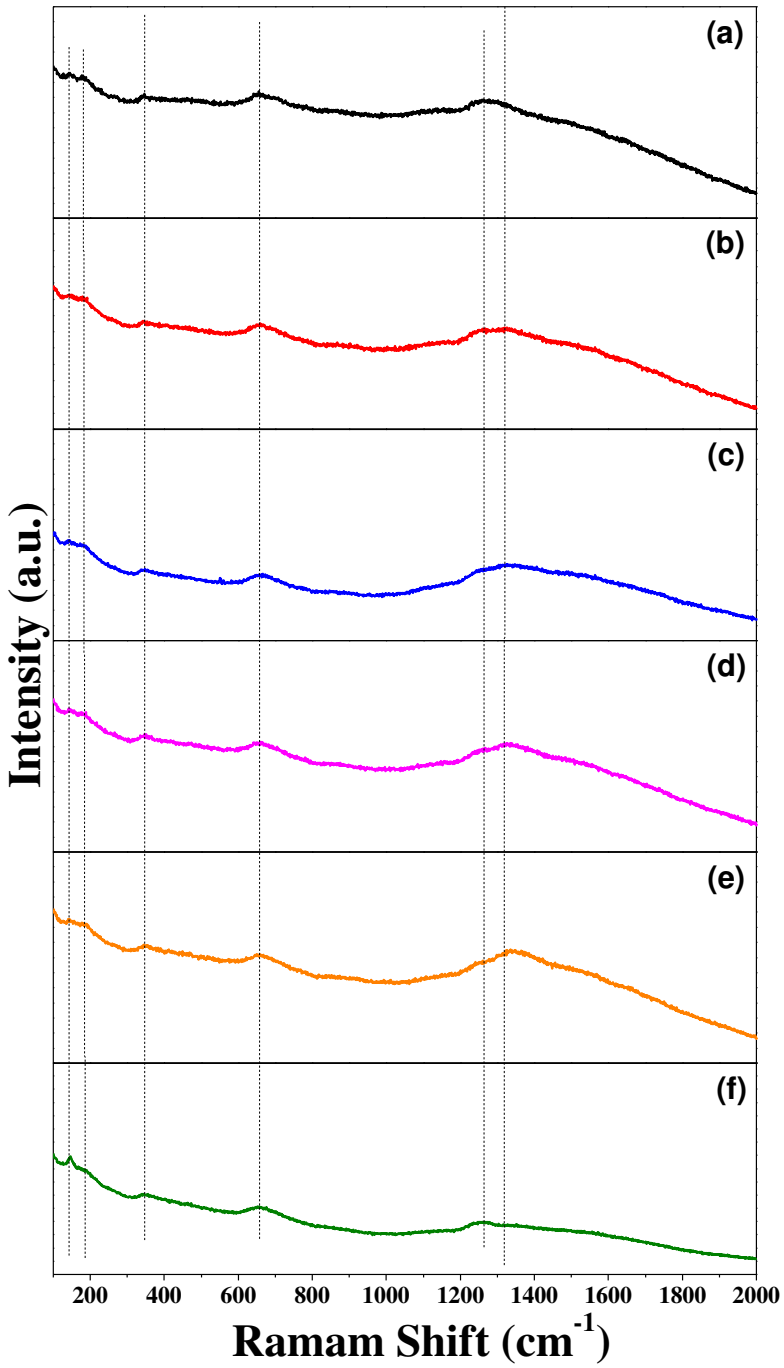

Fig. 5 Raman spectra of glass samples (a) GCNT0.1, (b) GCNT0.2, (c) GCNT0.3 (d) GCNT0.4, (e) GCNT0.5 and (f) GCNT0.7 respectively.

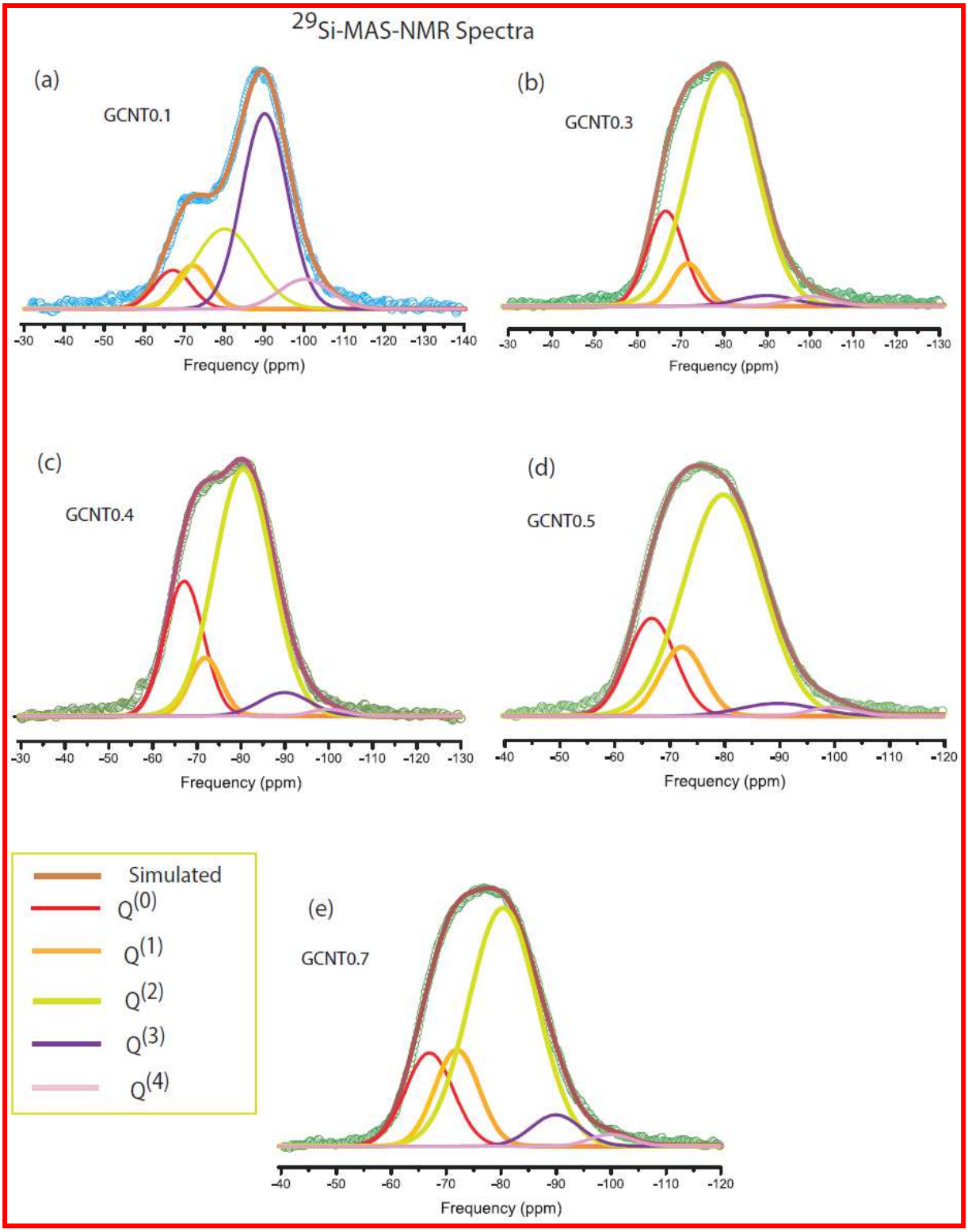

Fig. 6 ^{29}Si MAS NMR spectra of SiO_2-Al_2O_3-MgO-K_2CO_3-CaO-MgF_2-CNT with different fraction of CNT (a) GCNT0.1, (b) GCNT0.3, (c) GCNT0.4, (d) GCNT0.5, and (e) GCNT 0.7 respectively.

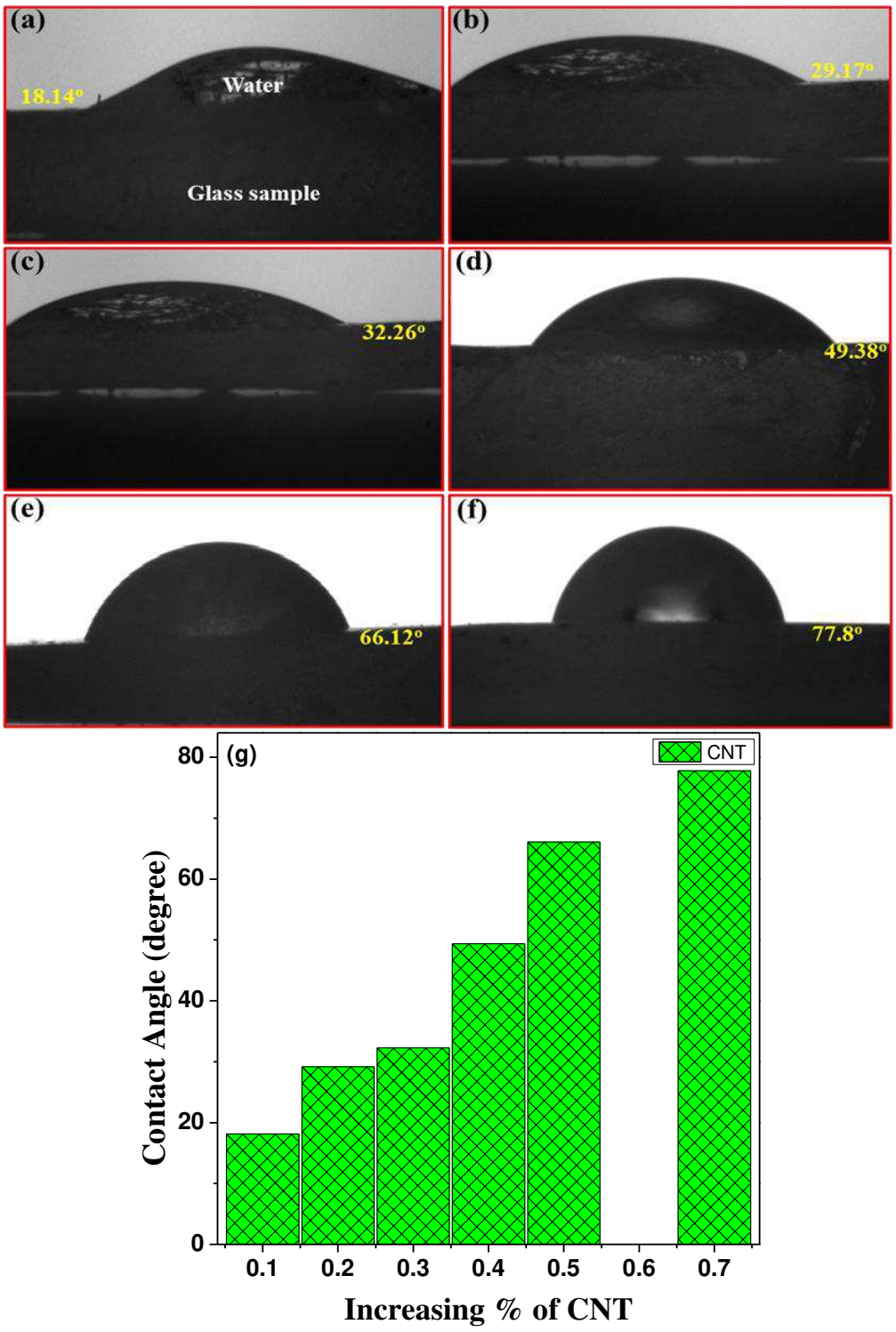

Fig. 7 Digital images shows the hydrophilic behavior of glass samples measured by optical images of contact angle calculated by image analyzer software (Image J) of the contact angle measurements of the different glass samples with water (a) GCNT0.1, (b) GCNT0.2, (c) GCNT0.3, (d) GCNT0.4, (e) GCNT0.5 (f) GCNT0.7 and (g) Variation of contact angle with increasing doping percentage of CNT.

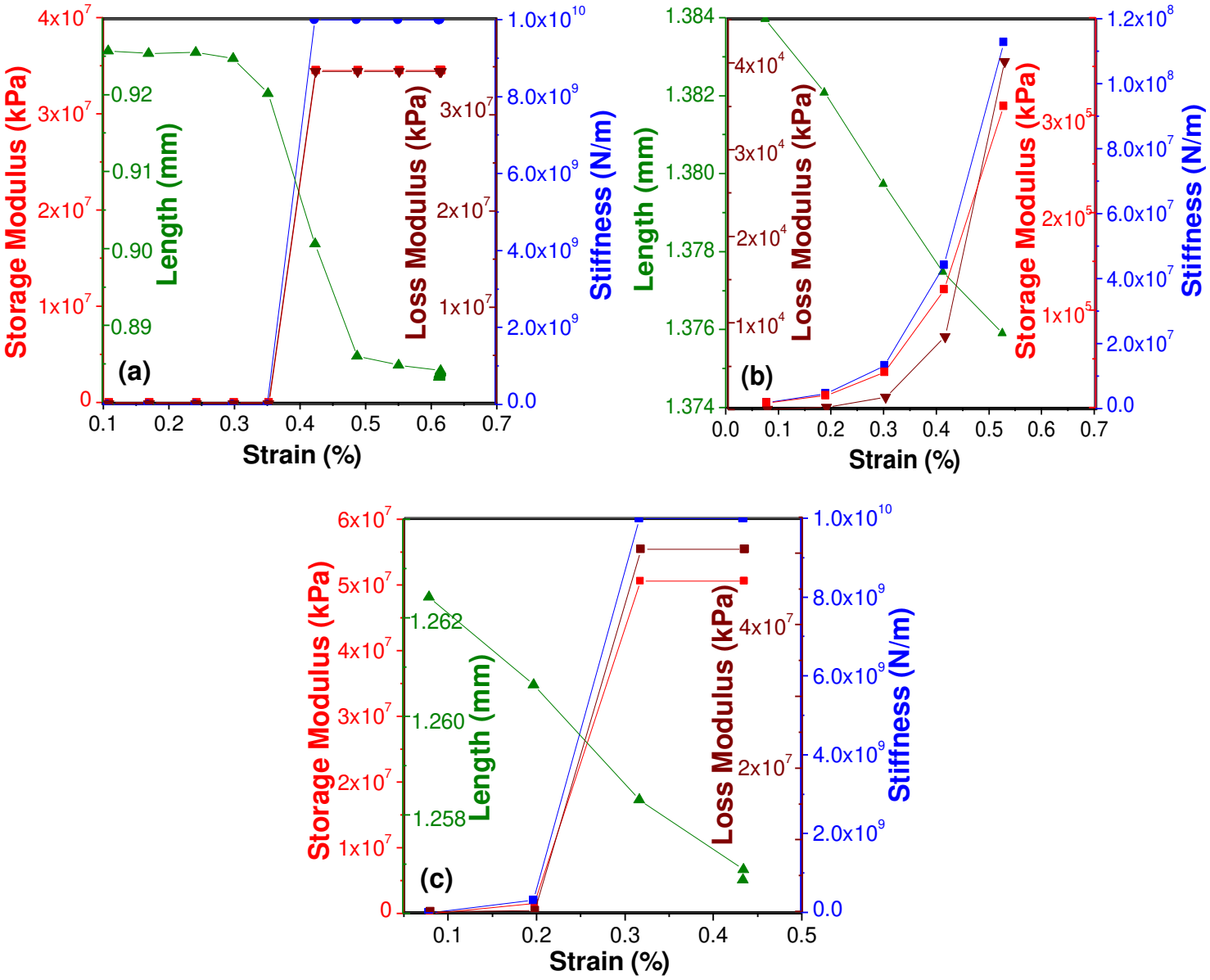

Fig. 8 Mechanical properties: variation of storage modulus, length, loss modulus and stiffness Vs strain percentage of the synthesized glass samples (a) GCNT0.1, (b) GCNT0.3 and (c) GCNT0.7 respectively.

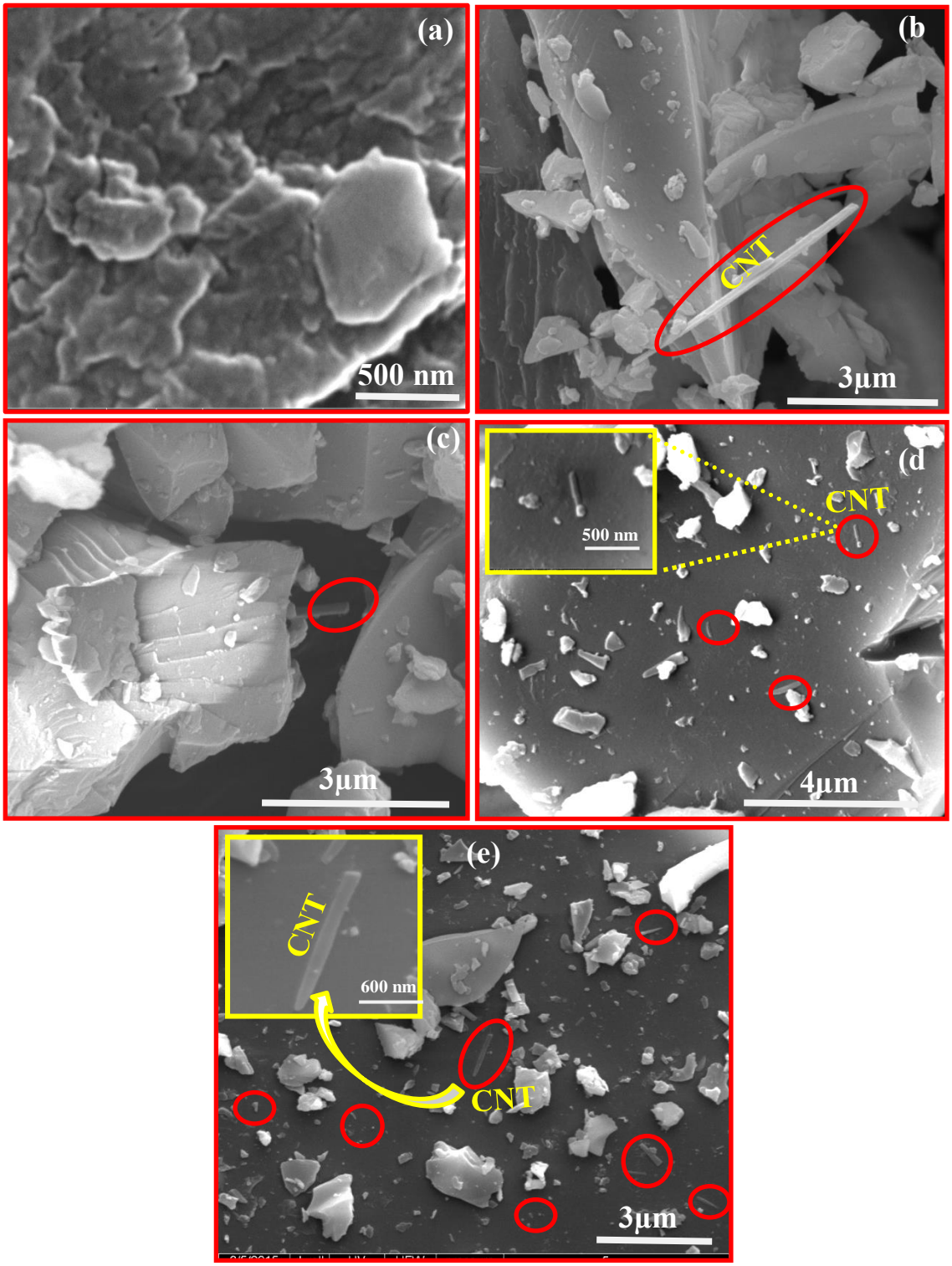

Fig. 9 Scanning electron micrographs of the powdered glass samples (a) GCNT0.1, (b) GCNT0.3, (c) GCNT0.4, (d) GCNT0.5, and (e) GCNT0.7 respectively.

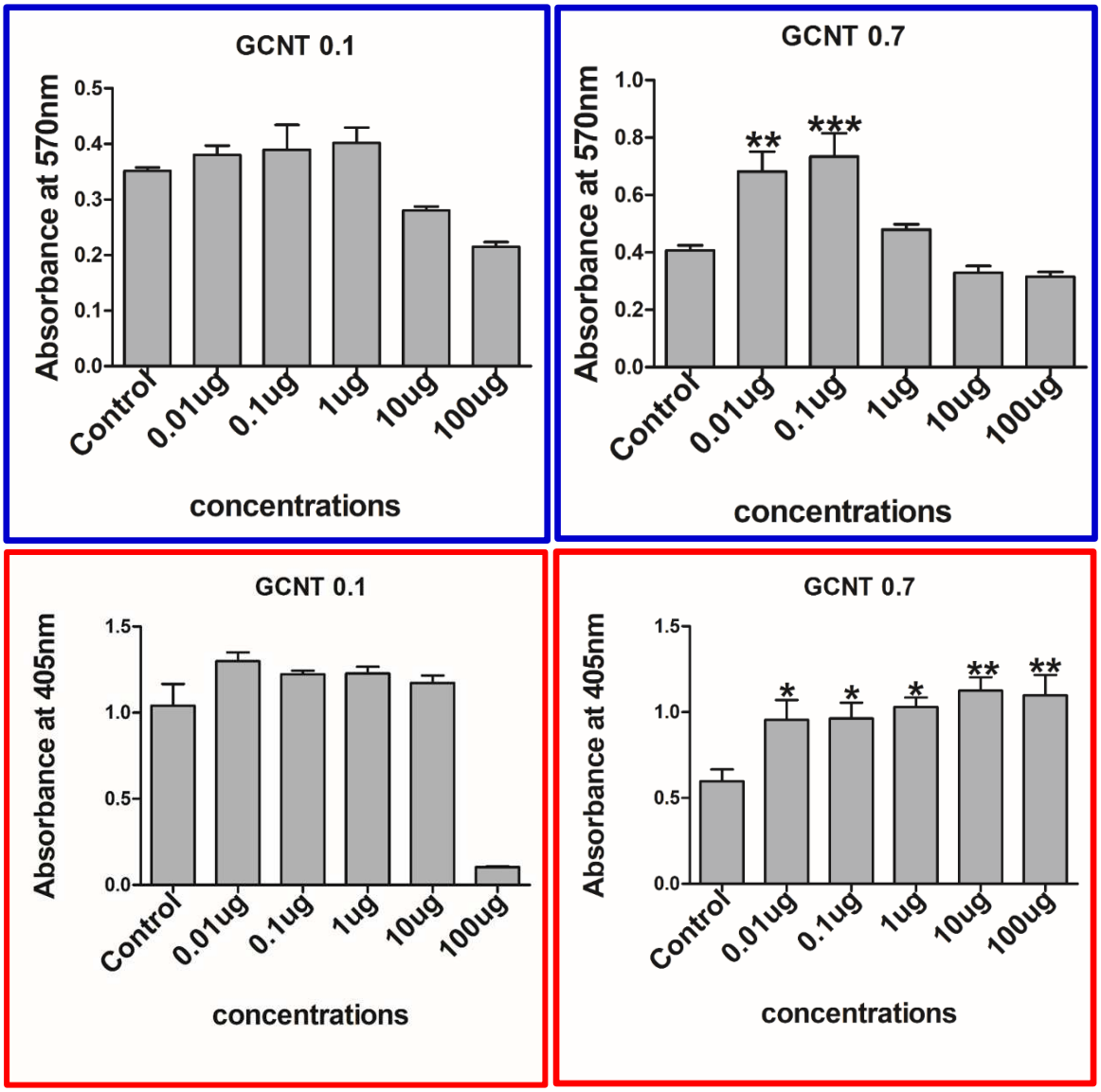

Fig. 10 Biological activities of CNT reinforced glass samples: (a & b) Cell viability (in terms of absorbance at 570 nm) of bioactive glass samples GCNT0.1 and GCNT0.7 with different concentrations (0.01–100 µg/ml), and (c & d) ALP activity of MCO cells treated with different concentrations of bioactive glass samples GCNT0.1 and GCNT0.7 with different concentrations (0.01–100 µg/ml).

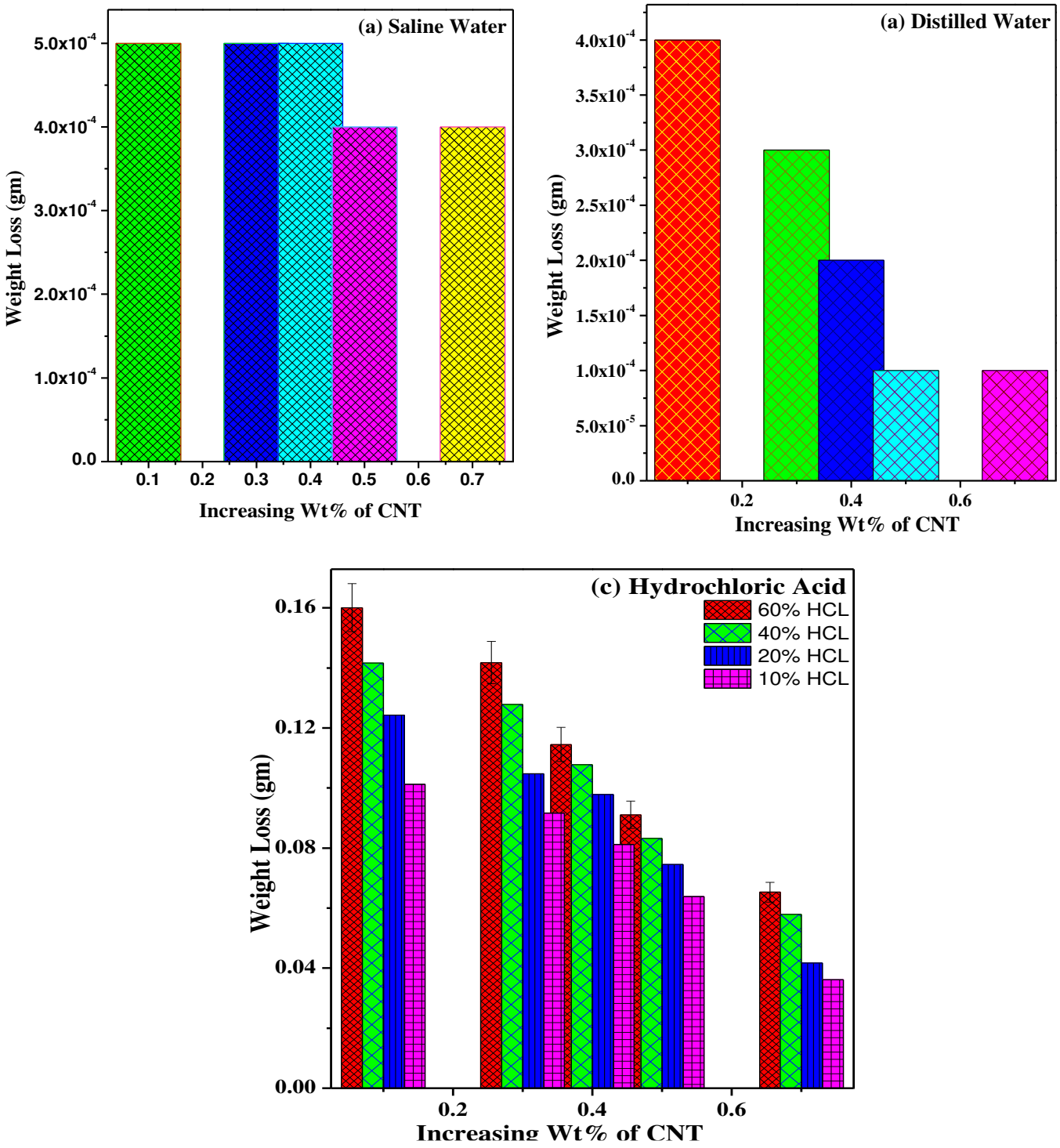

Fig. 11 Variation of weight loss in (a) saline water, (b) distilled water and (c) hydrochloric caid (HCL) Vs increasing weight percentage of CNT of the glass samples GCNT0.1, GCNT0.3, GCNT0.4, GCNT0.5, and GCNT0.7 respectively.

Figures

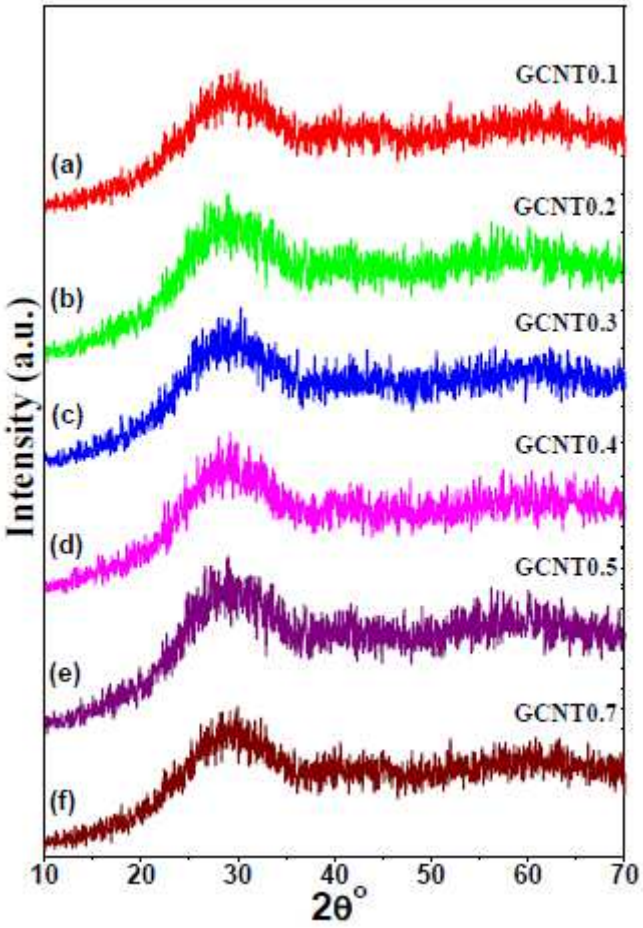

Figure 1

XRD patterns of the glass samples (a) GCNT0.1, (b) GCNT0.2, (c) GCNT0.3, (d) GCNT0.4, (e) GCNT0.5 and (f) GCNT0.7 respectively.

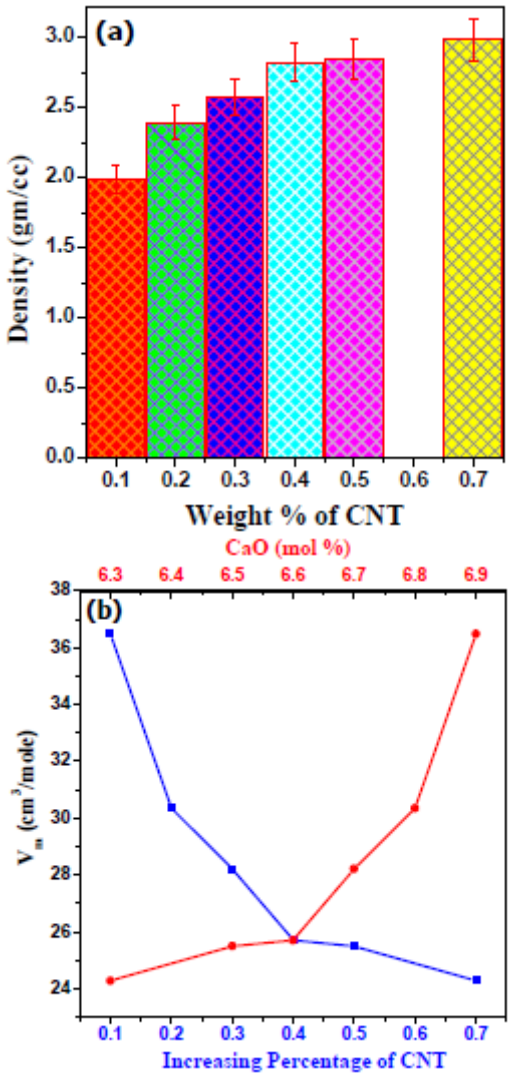

Figure 2

(a) Density of glass samples Vs reinforcement concentration of CNT and (b) Variation of molar volume Vs percentage of CNT and CaO.

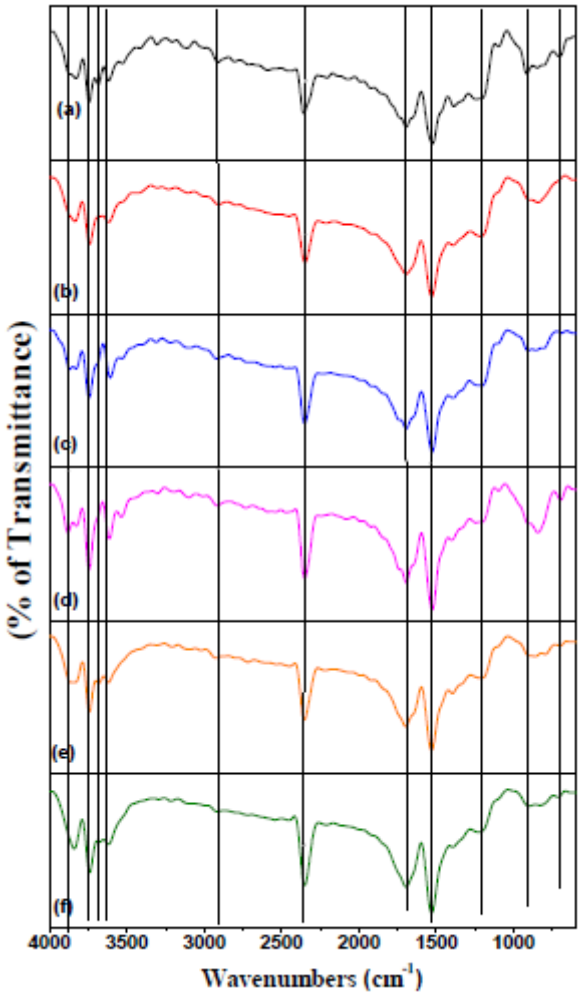

Figure 3

IR patterns of glass samples (a) GCNT0.1, (b) GCNT0.2, (c) GCNT0.3, (d) GCNT0.4, (e) GCNT0.5 and (f) GCNT0.7 respectively.

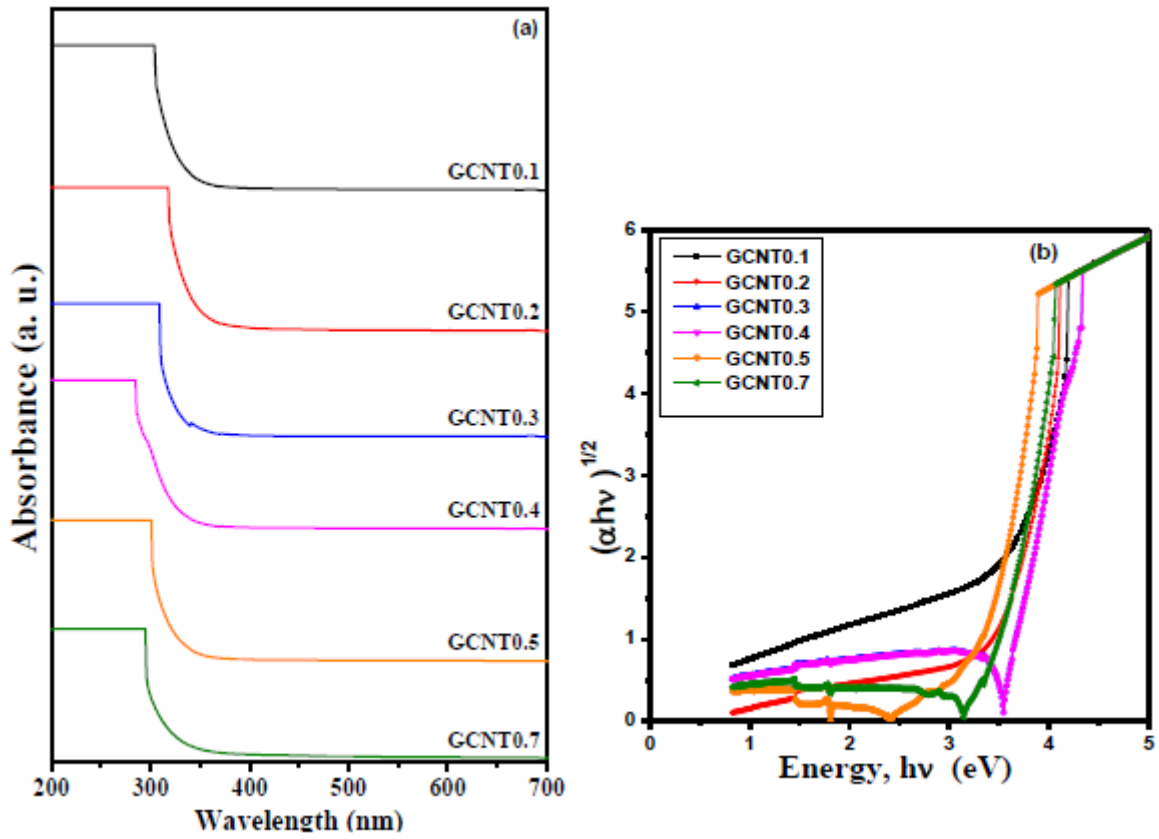

Figure 4

(a) UV-Vis spectra of glass samples GCNT0.1, GCNT0.2, GCNT0.3, GCNT0.4, GCNT0.5 and GCNT0.7 and (b) Davis and Mott plots of (αhv)1/2 versus hv of glass samples GCNT0.1, GCNT0.2, GCNT0.3, GCNT0.4, GCNT0.5 and GCNT0.7 respectively.

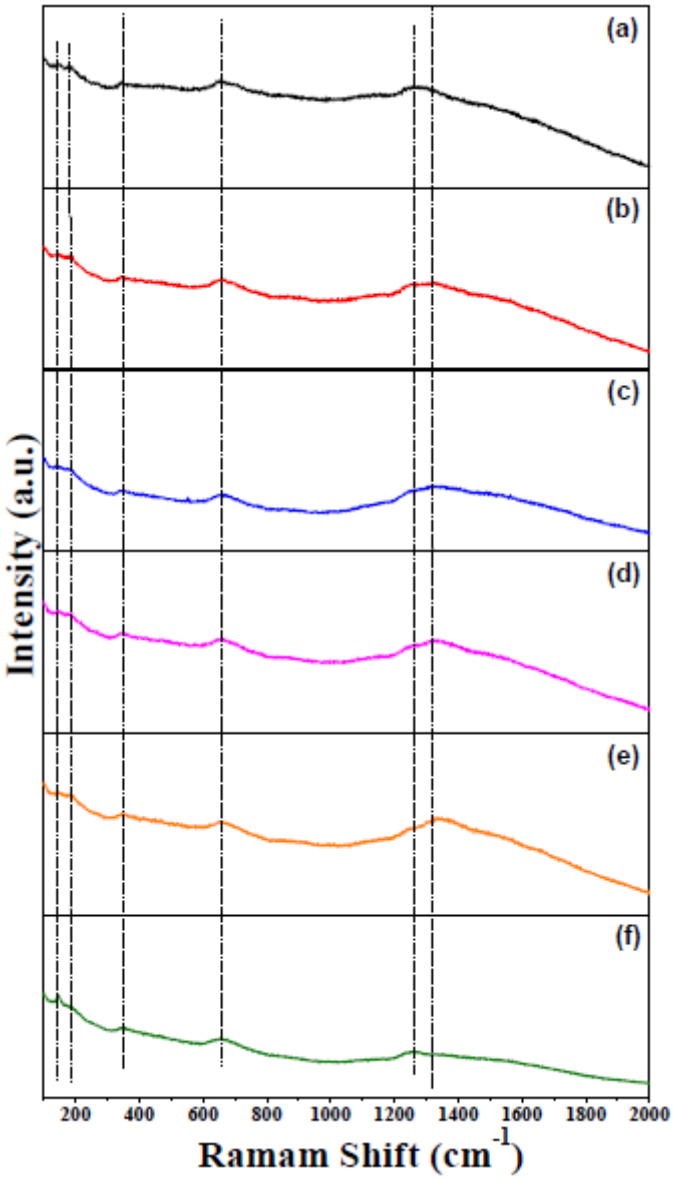

Figure 5

Raman spectra of glass samples (a) GCNT0.1, (b) GCNT0.2, (c) GCNT0.3 (d) GCNT0.4, (e) GCNT0.5 and (f) GCNT0.7 respectively.

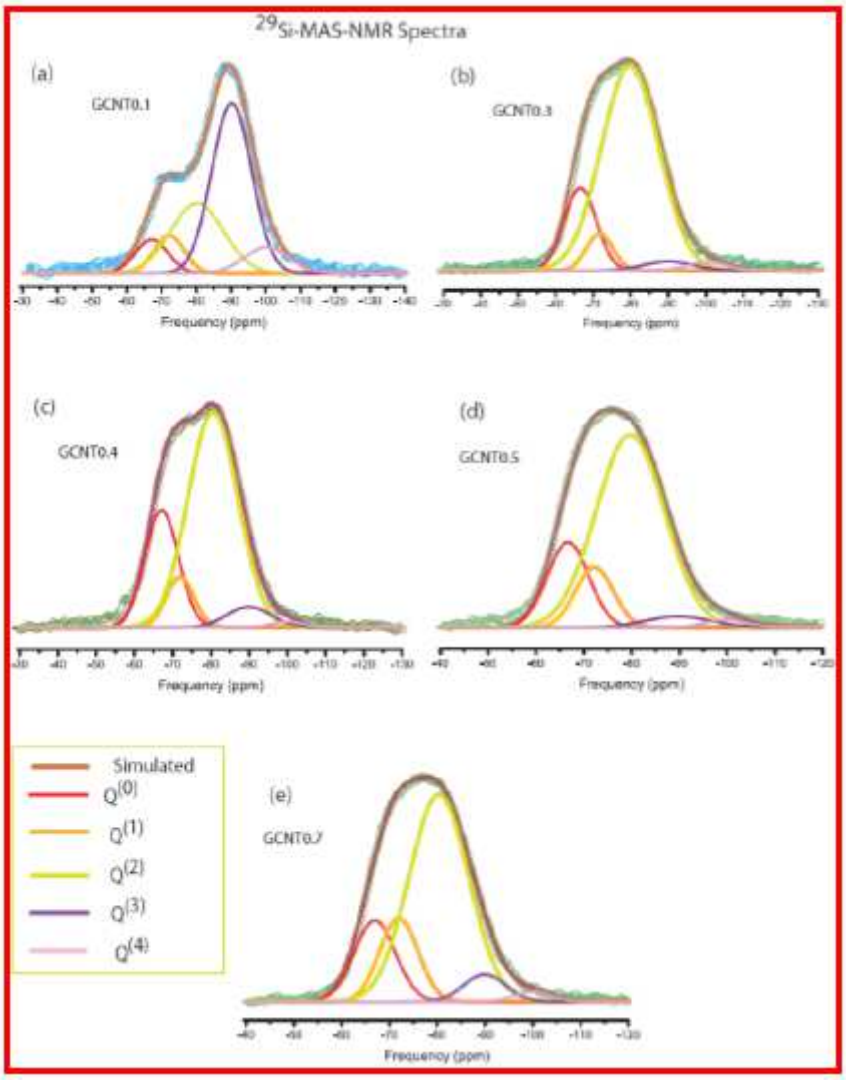

Figure 6

29Si MAS NMR spectra of SiO2-Al2O3-MgO-K2CO3-CaO-MgF2-CNT with different fraction of CNT (a) GCNT0.1, (b) GCNT0.3, (c) GCNT0.4, (d) GCNT0.5, and (e) GCNT 0.7 respectively.

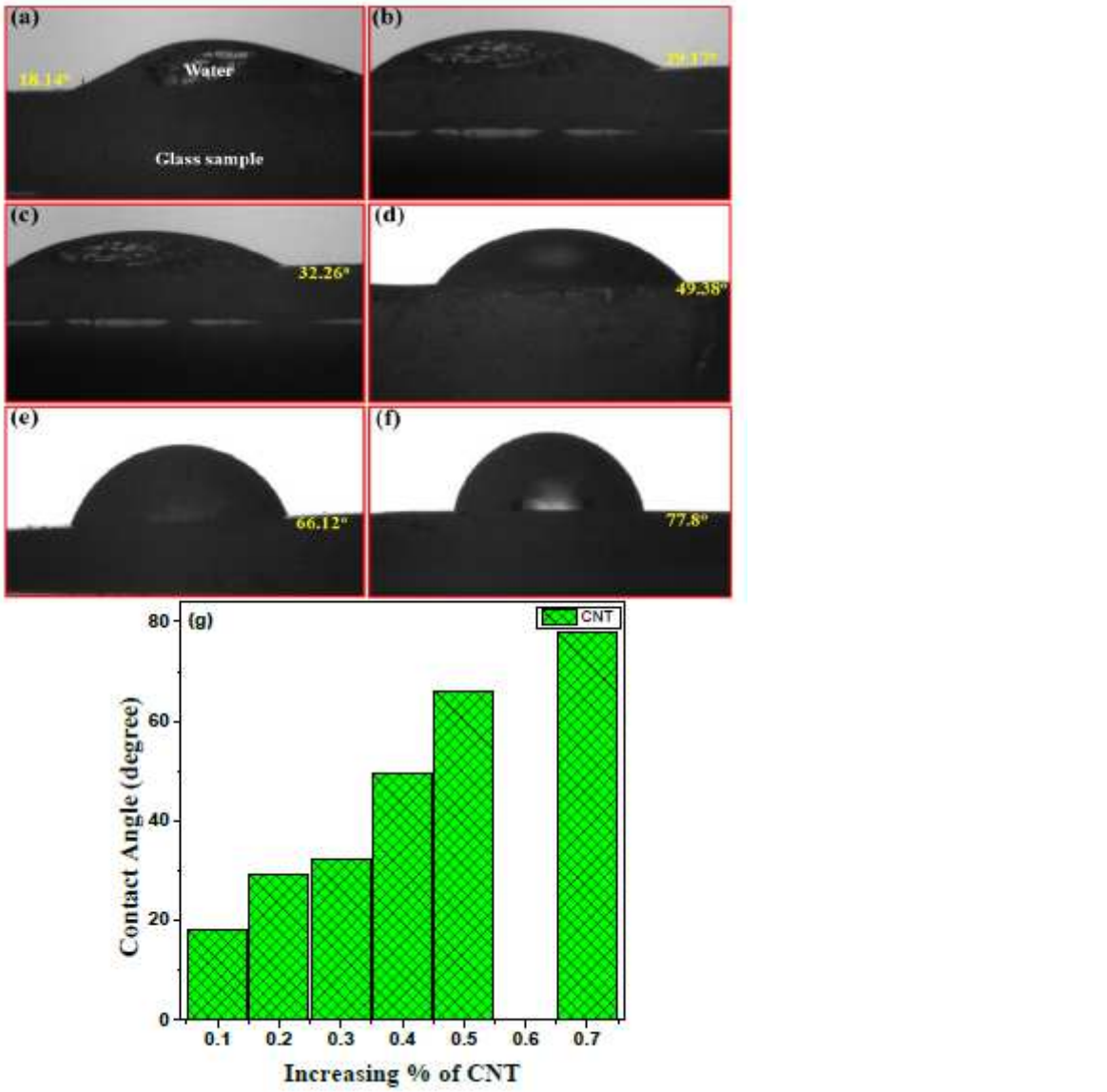

Figure 7

Digital images shows the hydrophilic behavior of glass samples measured by optical images of contact angle calculated by image analyzer software (Image J) of the contact angle measurements of the different glass samples with water (a) GCNT0.1, (b) GCNT0.2, (c) GCNT0.3, (d) GCNT0.4, (e) GCNT0.5 (f) GCNT0.7 and (g) Variation of contact angle with increasing doping percentage of CNT.

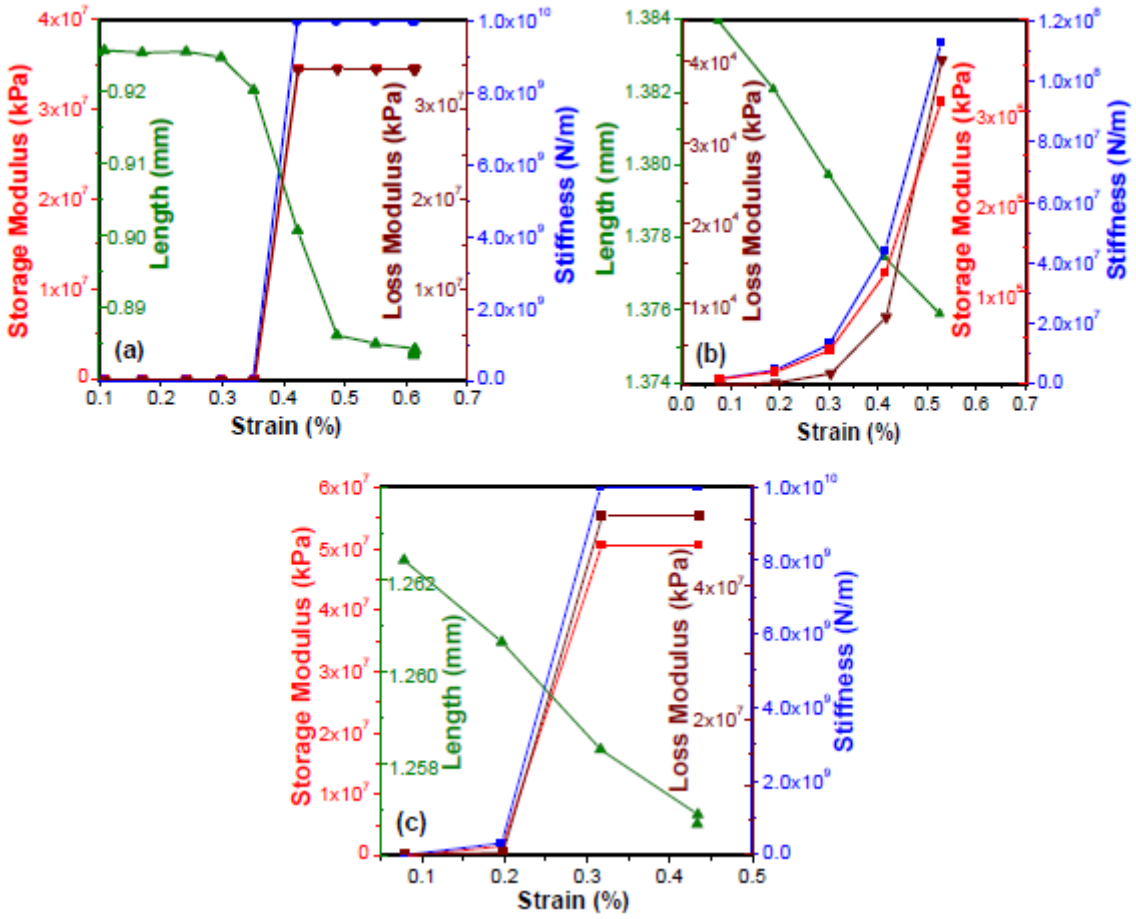

Figure 8

Mechanical properties: variation of storage modulus, length, loss modulus and stiffness Vs strain percentage of the synthesized glass samples (a) GCNT0.1, (b) GCNT0.3 and (c) GCNT0.7 respectively.

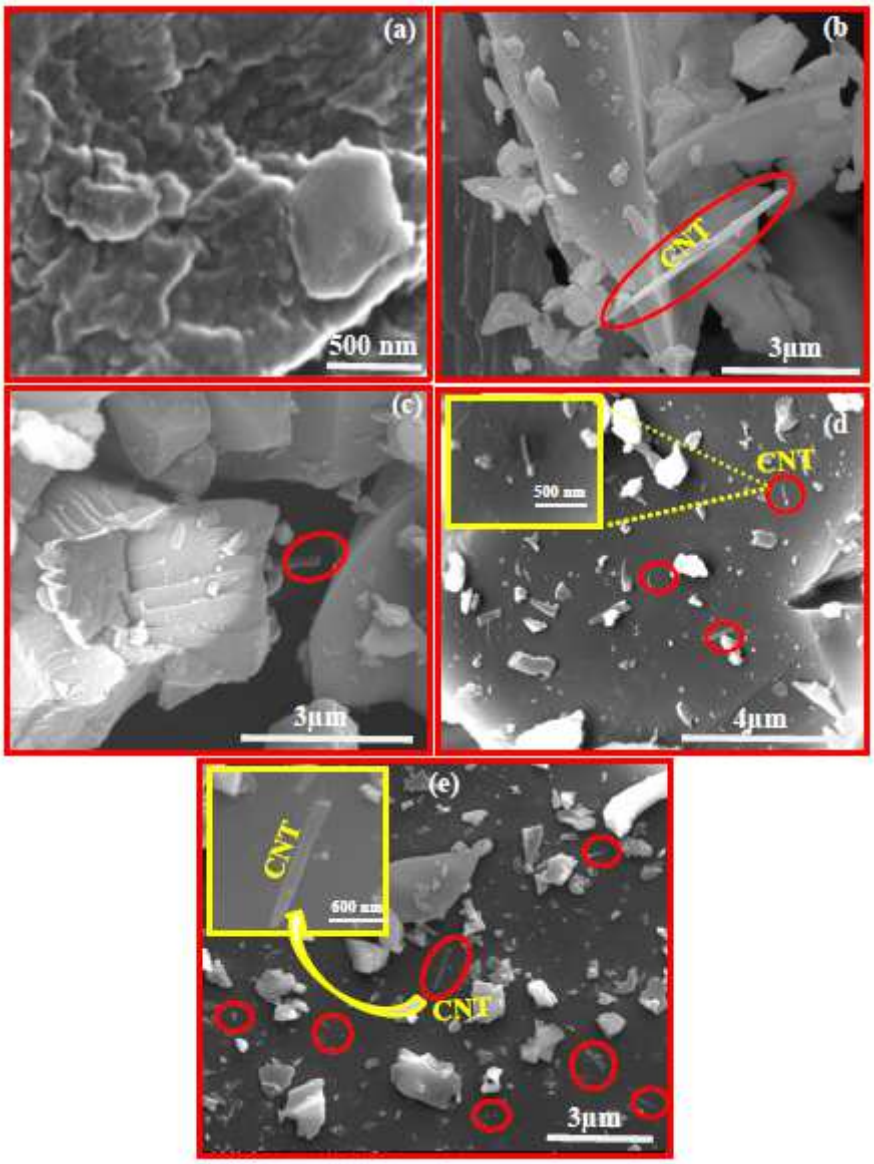

Figure 9

Scanning electron micrographs of the powdered glass samples (a) GCNT0.1, (b) GCNT0.3, (c) GCNT0.4, (d) GCNT0.5, and (e) GCNT0.7 respectively.

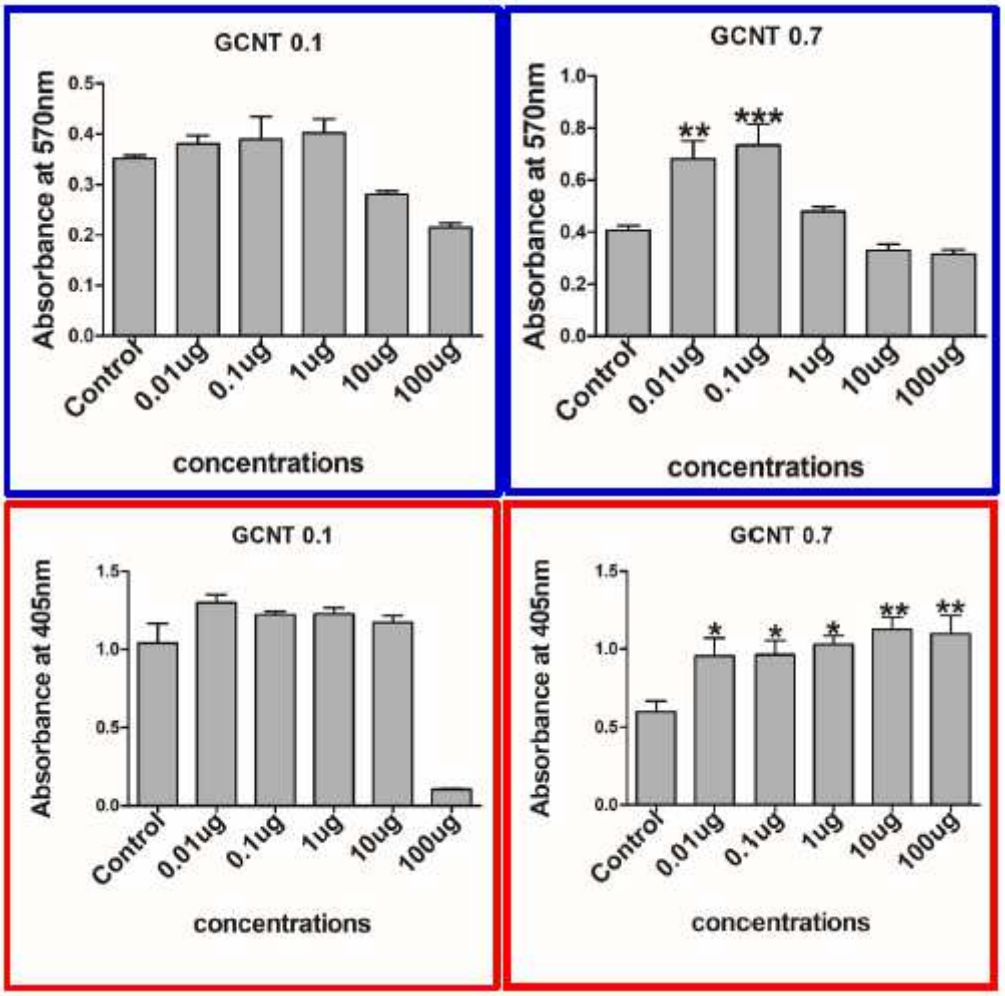

Figure 10

Biological activities of CNT reinforced glass samples: (a & b) Cell viability (in terms of absorbance at 570 nm) of bioactive glass samples GCNT0.1 and GCNT0.7 with different concentrations (0.01–100 μg/ml), and (c & d) ALP activity of MCO cells treated with different concentrations of bioactive glass samples GCNT0.1 and GCNT0.7 with different concentrations (0.01–100 μg/ml).

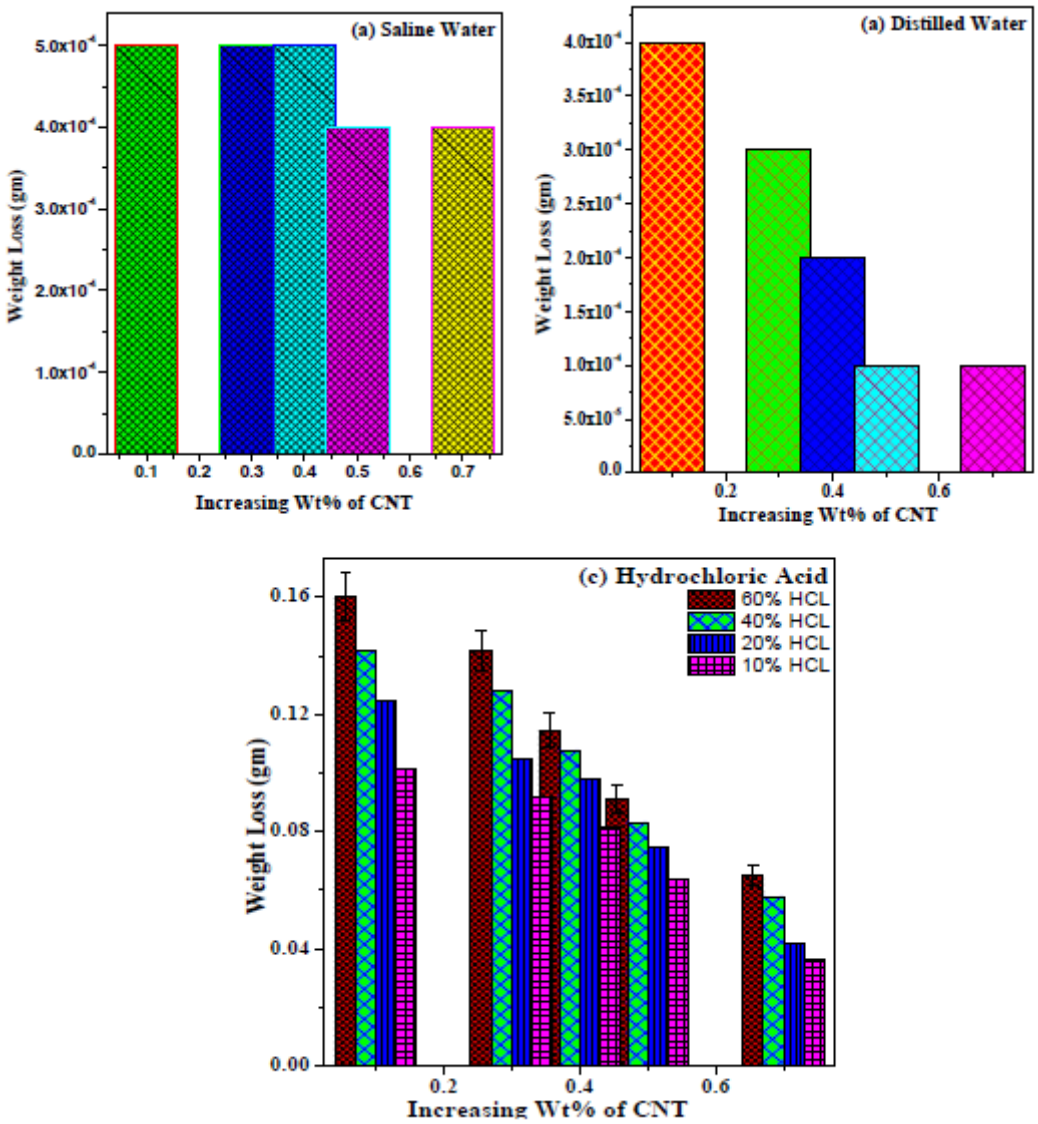

Figure 11

Variation of weight loss in (a) saline water, (b) distilled water and (c) hydrochloric caid (HCL) Vs increasing weight percentage of CNT of the glass samples GCNT0.1, GCNT0.3, GCNT0.4, GCNT0.5, and GCNT0.7 respectively.